Title

Characterizing fire and fire atmospheric states from space using collocated hyperspectral infrared sounding and narrow-band imagery

Authors

Zhou, Xuyang
Yue, Qing
Li, King-Fai
et al.

Publication Date

2024-10-01

DOI

10.1016/j.rse.2024.114318

Peer reviewed

Remote Sensing of Environment 312 (2024) 114318

Contents lists available at ScienceDirect

Remote Sensing of Environment

journal homepage: www.elsevier.com/locate/rse

Characterizing fire and fire atmospheric states from space using collocated hyperspectral infrared sounding and narrow-band imagery

Xuyang Zhou [a,b], Qing Yue [c,*], King-Fai Li [d], Evan Fishbein [c], Xiuhong Chen [e], Lin Tan [d], Sally Newman [a], Eric Fetzer [c], Yuk L. Yung [a,c]

[a] Divisions of Geological and Planetary Sciences, California Institute of Technology, Pasadena, CA, USA
[b] Computer Sciences, University of California, Los Angeles, CA, USA
[c] Jet Propulsion Laboratory, California Institute of Technology, Pasadena, CA, USA
[d] Department of Environmental Sciences, University of California, Riverside, CA, USA
[e] Department of Climate and Space Sciences and Engineering, The University of Michigan, Ann Arbor, MI, USA

ARTICLE INFO

Editor: Marie Weiss

Keywords:
Fire and associated environmental condition changes
Space-borne imagers and sounders

ABSTRACT

Under the influence of global climate change, wildfires are becoming increasingly significant within ecosystems. Satellite technology offers a critical perspective for studying fire. The synergy of high-spatial resolution narrow-band imagers and hyperspectral infrared (IR) sounders allow for comprehensive observation and long-term global monitoring of fire characteristics and associated atmospheric changes on the pixel scale. This study demonstrates methods to utilize the pixel-scale collocated fire observations from the Visible Infrared Imaging Radiometer Suite (*VIIRS*) and the IR radiance spectra from the Cross Track Infrared Sounder (*CrIS*), onboard NASA's Suomi National Polar-orbiting Partnership (SNPP) satellite, to analyze fire and the atmospheric conditions before, during, and after fires. Two months of satellite observations over the Southwest United States and the Amazonia regions when large fires occurred in the regions of interest (October 2017 and August 2020) are used. Our findings reveal that *CrIS* has high sensitivity to fire that affects as little as 1% of its field of view (FOV) with FOV total fire radiative power (FRP) larger than 200 MW (MW) at night and 1000 MW during the day. By employing spectral principal component analysis (PCA), the *CrIS* spectral signature to atmospheric temperature, humidity, and trace gases corresponding to fire characteristics are quantified. This approach highlights that collocated imager and IR sounder data, when paired with PCA, provide a powerful method to effectively identify and monitor wildfires. This technique also allows for the observation of subsequent atmospheric alterations while managing data volume efficiently, ensuring that crucial spectral information is preserved. This methodology advances our ability to understand and respond to the multifaceted impacts of wildfires on both local and global scales, reinforcing the value of integrated satellite observations in environmental science.

1. Introduction

Fire is an important integral process within the Earth system that has profound influences on the structure of ecosystem and atmospheric composition. In the absence of human influence (e.g., agricultural activities), fire naturally recycles carbon between soil and vegetation on the time scale of 30–40 years related to tree growth (Watson et al., 2000). In this process, gaseous carbon compounds, primarily carbon monoxide and carbon dioxide, are also released to the atmosphere. In the last few decades, however, global wildfire occurrences have been undergoing unprecedented changes due to a combination of natural (e.g., natural variability at different scales) and human-induced (e.g., forest and water resource management and anthropogenic climate change) drivers on climate and ecosystems, marked by increasing magnitude and frequency of fire weather, fire events, and the duration of the fire season, which brought profound social and economic impacts (Abatzoglou et al., 2019; Abram et al., 2021; Bowman et al., 2017; Flannigan et al., 2009; Jain et al., 2022; Kelley et al., 2019; Touma et al., 2021). Therefore, observations of both the fire characteristics and the associated atmospheric environmental changes are essential to fully understand the fire physical processes, the feedback mechanisms, and their impacts on the Earth System, for which the synergy of satellite imagers with high spatial

* Corresponding author.
E-mail address: qing.yue@jpl.nasa.gov (Q. Yue).

https://doi.org/10.1016/j.rse.2024.114318
Received 1 March 2024; Received in revised form 9 July 2024; Accepted 10 July 2024
Available online 20 July 2024

resolution and sounders with high spectral resolution provides a multi-decadal global data record from space.

In recent decades, a critical advance in fire science is the development and applications of operational satellite products. Visible and infrared (IR) narrowband imagers, which offer a high spatial resolution but coarse spectral resolution, have been widely used in detecting and monitoring fires at different sizes and strengths from space. Multiple narrowband imagers are currently operating in Low Earth Orbit (LEO) and on geostationary (GEO) platforms, such as the Advanced Very High Resolution Radiometer (*AVHRR*, since 1979), Moderate Resolution Imaging Spectroradiometer (*MODIS*) aboard NASA's Earth Observing System (EOS) Terra and Aqua satellites (since 1999 and 2002, respectively), Visible Infrared Imaging Radiometer Suite (*VIIRS*) aboard the Suomi National Polar-orbiting Partnership (SNPP, since 2011), and NOAA's new generation of Joint Polar Satellite System (JPSS) satellites (since 2017). Active fires are detected by these instruments as heat anomalies by the spectral signature of fire-affected land surfaces by combining information from their visible and IR channels (Chuvieco and Martin, 1994; Flasse and Ceccato, 1996; Giglio et al., 2003, 2016; Morisette et al., 2005; Schroeder et al., 2008; Wooster et al., 2003; Yu et al., 2024). Specifically, the continuity effort of *MODIS* and *VIIRS* ensures a well-established long-term active-fire data product providing information on location, emitted energy, the flaming and smoldering ratio of fire, and estimate of the burnt area. However, the coarse spectral resolution of these imagers limits their capability to monitor the detailed vertical structure of the fire emissions and fire weather conditions such as thermodynamic properties before, during, and after fire. These are key parameters to understand the interactions between the Earth System and fires (Field et al., 2015; Flannigan et al., 2016; Jain et al., 2022), and to predict the short-term and long-term fire danger globally and regionally (Farahmand et al., 2020; Wang et al., 2017).

Space-borne hyperspectral IR sounders, often flying in concert with the narrowband imagers on operational environmental satellites, have the capability to measure spectra at high spectral resolution (< 1 cm^{-1}) usually at a spatial resolution of ~15 km. These operational IR sounders also cover the shortwave-IR region for fire detection, although its applicability is limited by the coarse spatial resolution. No quantitative analyses on the operational sounder fire sensitivity limit have been carried out. On the other hand, the capability and information content of hyperspectral IR sounding is strongly dependent on the atmospheric and surface states of the observed scene (Yue et al., 2011; Yue et al., 2013; Yue and Lambrigtsen, 2019). As fire weather is often associated with dry and less cloudy conditions, the IR spectral measurements have good capability to record the entire atmospheric column profiles. Therefore, the IR sounders could provide critical information on the vertical and spatio-temporal features of the environmental changes associated with fire including both thermodynamic conditions and trace gases, which often have a much larger spatial scale than the fire itself.

Major US and European LEO operational environment satellites carry both narrowband imagers and hyperspectral IR sounders (together with microwave sounders), such as the AVHRR and Infrared Atmospheric Sounding Interferometer (*IASI*) on multiple Meteorological Operational (MetOp) satellites, *MODIS* and the Atmospheric Infrared Sounder (*AIRS*) on Aqua, and *VIIRS* and the Cross Track Infrared Sounder (*CrIS*) carried on the SNPP and JPSS satellites. The synergy of imagers and sounders with a multi-decadal global coverage provides the capability to observe and monitor both the short- and long-term aspects of fire events and fire environmental change from space. However, the sheer volume of these datasets and their different granulization pose a bottleneck for the community.

In this work, we combine the instantaneous measurements of imagers and sounders to simultaneously utilize the quantitative information on fire characteristics from imagers, and the high-resolution spectral signature of sounder observations associated with large-scale atmospheric variations in, e.g., atmospheric temperature, humidity, and trace gases during and immediately before/after fire events.

The huge volume of raw hyperspectral sounding data to be involved demands tremendous computational power that makes real-time applications inefficient. One approach may reduce the data volume by preselecting a subset of channels that is representative of the surface heat anomaly and absorption features of some target quantities such as water vapor and carbon monoxide. Another approach is to reduce the data dimensionality by truncating the leading principal components (PC) that are representative of various atmospheric conditions using spectral principal component analysis (PCA) while the full spectral information could still be retained with reduced measurement noise. Both approaches are explored in our study to 1) provide a quantitative analysis on sensitivity of hyperspectral IR sounder observations to fire and fire environmental conditions; 2) build a dataset describing both fire and fire weather in before, after, and during fire conditions, and 3) test out a fast method for real-time fire weather monitoring from space using multi-sensor observations.

The spectral PCA method relies on the interchannel covariance of the absorption features across the spectrum (Antonelli et al., 2004; Huang and Antonelli, 2001). The applicability of PCA to problems of data compression and suppression of instrument random noise, inversion, and extreme event detection has been studied and deployed in mission data processing for multiple hyperspectral IR sensors on both space-borne and ground platforms (Goldberg et al., 2003; Lee et al., 2019; Serio et al., 2020; Tobin et al., 2007; Tremblay et al., 2022; Turner et al., 2006) including *AIRS*, *CrIS*, *IASI*, and the Atmospheric Emitted Radiance Interferometer (*AERI*), and has also been used to identify extreme events (Hultberg et al., 2017; Vu Van et al., 2023). However, it remains a challenge to retain spectral signals associated with sporadic extreme events, such as wildfires, due to lack of sufficient training datasets. Intuitively, the minimum number of PCs needed to retain a target signal depends on whether and how much prior data of the target signal has been used during the training. Atkinson et al. (2010) showed that including as few as 10% of the *IASI* spectra in the training dataset for a prior volcanic eruption event would tremendously improve the reconstruction of the spectral signatures of methane (CH_4), CO, ammonia (NH_3), and sulfur dioxide (SO_2) of posterior volcanic eruption events using IASI observations. Therefore, to preserve full spectral information from sounders for operational applications, it is important to develop new methods that could identify rare or extreme events and include them in the training datasets. On the other hand, a truncated set of PCs obtained from a training dataset built only on normal conditions, e.g., an environment with insufficient representation of extreme events such as fires, would show large errors when they are used to reconstruct the spectra of extreme events. Such spectral reconstruction "errors" could be used to develop real-time application tools for detecting extreme events. Thus, in this study the instantaneous collocated imager observations are used to quantify the detailed fire characteristics for each radiance spectrum from hyperspectral sounders and then analyze and compare the results of PCA applied to the spectra composited by fire conditions.

To demonstrate our method, the pixel-scale collocated *CrIS* and *VIIRS* observations on the SNPP satellite are used. *CrIS* and *VIIRS* are the imager-sounder pair that will operate on the US LEO environmental satellites until ~2050, providing long-term continuity observations of Earth's climate. The vertical profiles of temperature and water vapor from the 5th generation global atmospheric reanalysis from the European Centre for Medium-Range Weather Forecasts (ECMWF), ERA5.1, are also collocated with satellite observations to facilitate the analysis of the spectra. We describe the data and methodology in Section 2. We then discuss our results in Section 3 and present concluding remarks in Section 4.

2. Data and methodology

Using the pixel-scale collocated SNPP *CrIS* and *VIIRS*-750 m index data (Fetzer et al., 2022), the Version 1 SNPP-*VIIRS* Thermal Anomalies/Fire 750 m Level 2 (L2) products (VNP14) are matched with the Version

3 SNPP-*CrIS* Level 1B (L1b) radiances at the native resolution of *CrIS* (14 km at nadir). The *CrIS* fields of view (FOVs) are categorized into three groups: during-fire for which an active fire is identified by VNP14 within the *CrIS* FOV, before-fire and after-fire that are fire-free *CrIS* FOVs within five days before and after an active fire identified at the same location, respectively. The active burning areal percentage of the *CrIS* FOV and the fire radiative power (FRP, Kaufman et al., 1996, Wooster et al., 2003) are calculated from the collocated *VIIRS* fire retrievals. More details are given in the following sections and the Appendix.

2.1. Study regions and time periods

We will focus on two regions with distinct climate regimes, the southwestern United States (SWUS, 32°N–42°N, 235°E–246°E) and Amazonia (20°S–10°N, 280°E–320°E) as shown in the boxes in Fig. 1. These two regions represent drastically different climate and biogeographical regimes, causing significantly different relationships between fire activity and fire weather, contributed by both natural and human factors. Yet both regions are deeply impacted by increasing disturbance from fires while enduring significant upward trends in fire weather due to changes in climate and ecosystem (Andela et al., 2019; Jiang et al., 2021; Jones et al., 2022).

Fires in SWUS often occur in the coastal mountainous regions. This region tends to have lower levels of atmospheric moisture compared to other regions due to its arid and semi-arid climate. The *AIRS* data show that the mean total column water vapor (TCWV) concentrations in SWUS range from 10 to 20 mm (mm) and 5–15 mm during the summer and winter months, respectively (not shown). Fires in Amazonia are often associated with deforestation and occur dominantly in Amazonia's dry season, when the mean TCWV ranges from 20 to 40 mm, which is much wetter than the SWUS annual mean. Such regime differences are also valuable to address the scene-dependence of the IR sounder information content (Yue and Lambrigtsen, 2019).

Two months of data, October 2017 and August 2020, are used in this study, which are the typical fire seasons in Amazonia and SWUS.

2.2. SNPP-VIIRS thermal anomalies/fire 750-m level 2 (version 1): VNP14

The fire mask layers in SNPP-*VIIRS* Thermal Anomalies/Fire 750-m Level 2 (L2) products (VNP14) are used to identify pixels with active fire events. Each VPN14 L2 file contains a 6-min orbital segment of thermal anomalies and fire retrievals at 750-m resolution from the SNPP-*VIIRS* instrument. The retrieval algorithm is adapted from the *MODIS* Collection 6 Fire and Thermal Anomalies product (Giglio et al., 2016) so the VPN14 product provides a continuation of the 1-km EOS-*MODIS* active fire data record (Schroeder and Giglio, 2017). Six 750-m *VIIRS* channels are used as the input to the algorithm to provide cloud, surface classification, sun glint, fire detection, and quality assurance. The main input is the *VIIRS* M13 channel at 4 μm. Compared to *MODIS*, the higher spatial resolution of *VIIRS* fire products increases the sensitivity of *VIIRS* to smaller fires. The dynamically assigned low/high gain setting of the M13 channel increases the saturation temperature of the channel to 659 K compared to 500 K of the *MODIS* Channel 21. As a result, pixel saturation of the *VIIRS* 750-m 4-μm channel is very rare except for extremely large and intense fires (Schroeder and Giglio, 2018). After assessment using ground truth information from field campaigns (Dickinson et al., 2016) and qualitative same-day Landsat-class data corroborated by user feedback (Oliva and Schroeder, 2015), the *VIIRS* fire product is currently given a status of validated maturity.

The VPN14 FRP is retrieved using the radiance approach developed by Wooster et al. (2003) and Wooster et al. (2012) which still needs

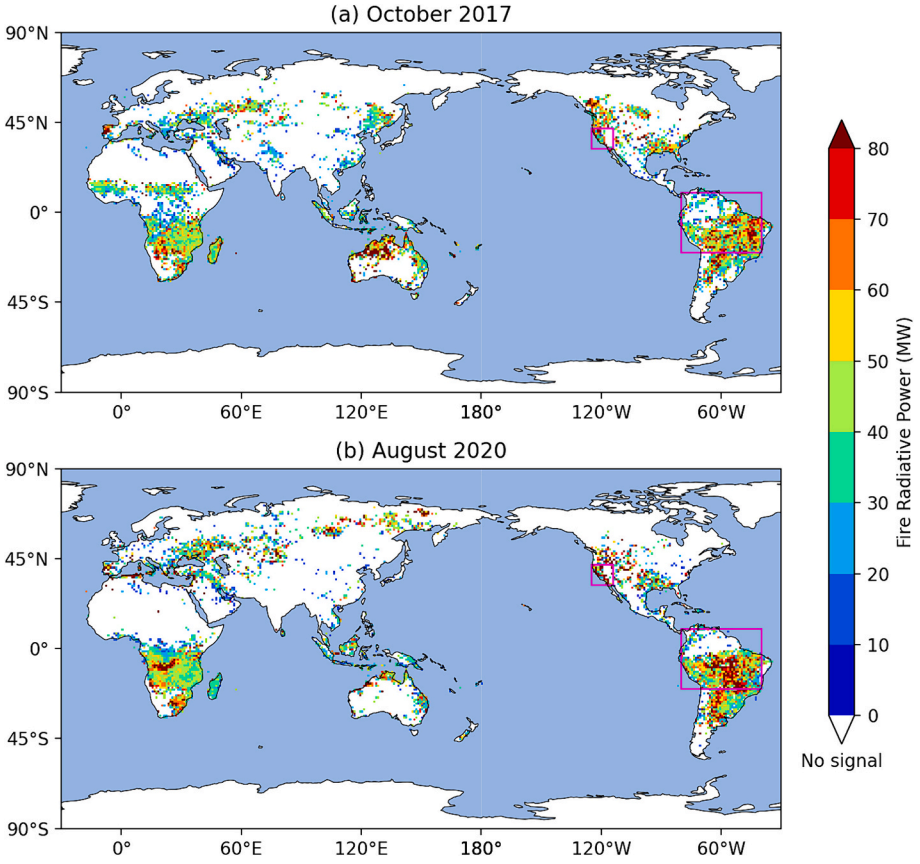

Fig. 1. *VIIRS* mean fire radiative power map on 1° × 1° latitude by longitude grid box from the two months of data with the boxes showing the two selected regions: Amazon and Southwestern United States (SWUS). Only observations over land are used in this study.

more verification and validation analyses (Schroeder and Giglio, 2017). This study uses the VPN14 FRP retrievals as a qualitative indicator to characterize the strength of the fire, given uncertainties associated with its retrieval, especially for intense fires due to channel saturation or for small fires due to the resolution and detection limit of the *VIIRS* 750-m channels. Fig. 1 shows the *VIIRS* FRP averaged on $1^\circ \times 1^\circ$ grids from the two months of observations, with the two selected focus regions enclosed in the rectangular boxes (only observations over land are used).

2.3. SNPP-CrIS level 1B (L1B) full spectral resolution (FSR) version 3

The SNPP-*CrIS* L1B spectral radiances at the full spectral resolution (FSR) are used to characterize the signature of wildfires as well as the associated environmental changes. Each SNPP-*CrIS* L1B FSR file contains unapodized radiance measurements over one 6-min orbital segment (i.e., a granule) and there are 240 granules per day. The SNPP-*CrIS* FSR product has high spectral resolution of 0.625 cm^{-1} (unapodized) in three IR bands: the long-wave IR band 1 (648.75–1096.25 cm^{-1}), the mid-wave IR band 2 (1208.75–1751.25 cm^{-1}), and the short-wave IR band 3 (2153.75–2551.25 cm^{-1}) (Han et al., 2013, Revercomb and Strow, 2020). Radiance measurements from a total of 2223 spectral channels are provided at a spatial resolution of approximately 14 km at nadir. The Noise Equivalent Differential Radiance (NEDN) for each channel is also reported by granule in the L1B product, which is a key parameter describing the *CrIS* instrument noise (Zavyalov et al., 2013; Tobin et al., 2013).

2.4. Pixel-scale collocated CrIS and VIIRS observations for fire science: SNPP CrIS–VIIRS 750-m matchup indexes version 1

The collocated SNPP *CrIS* and *VIIRS* index products (SNPP_*CrIS*_*VIIRS*750m_IND) developed through NASA's Making Earth Science Data Records for Use in Research Environments (MEaSUREs) program are used (Fetzer et al., 2022) to take advantage of the synergistic observations of imagers and sounders (Wang et al., 2016). The L2 VPN14 fire observations and *CrIS* L1B hyperspectral IR radiances are matched at the pixel scale following the method in Yue et al. (2022) using the collocation index product (see Appendix for more details). The characteristics of fires from the finer-resolution *VIIRS* pixels are collected and summarized within a given *CrIS* FOV where IR spectra to retrieve atmospheric thermodynamic and emission conditions are measured.

The during-fire observations are first selected from the two months of data over each of the two regions. The location and time of the fire, the fire size (spatial coverage), and the total FRP in the *CrIS* FOV (fire strength) are recorded by summarizing the fire information within each *CrIS* FOV reported in the collocated *VIIRS* active fire product. To quantify the sensitivity of *CrIS* spectra to fire characteristics, the fire size is simply calculated as the ratio (in percent) of *VIIRS* active fire 750-m pixels to the total number of *VIIRS* 750-m pixels that are collocated within one given *CrIS* FOV. The before- and after-fire *CrIS* FOVs are then selected using the criteria discussed previously: fire-free by *VIIRS* observations and within the five-day time window before or after an active fire was identified at the same location. Each group is then divided into day- (local solar time from 8 am to 4 pm) and night-time (local solar time from 9 pm to 4 am) observations to separate the following factors from the spectral sensitivity to fire and fire weather: 1) the solar radiance impact on the shortwave-IR channels and 2) the algorithm differences between day- and night-time *VIIRS* active fire retrievals. From the two months of data, there are 592 and 150 day- and night-time *CrIS* fire FOVs that have the before and after fire FOVs available in the SWUS region. The Amazonia region has 14,672 and 3647 *CrIS* fire FOVs satisfying the criteria during day- and night-time, respectively.

2.5. ERA5.1 temperature and water vapor profiles matched to satellite observations

Produced using a 4D-Var data assimilation, ERA5 has a much higher spatial and temporal resolution than its predecessor, ERA-Interim (Hersbach et al., 2020). In addition, newly reprocessed datasets along with recent instruments (such as *CrIS*) have been assimilated into ERA5 that could not be ingested into ERA-Interim (Hersbach et al., 2019; Hennermann and Berrisford, 2020). ERA5 atmospheric fields have been used extensively in studies of fire weather and fire danger (Vitolo et al., 2020). Although reanalysis data may not accurately represent the point location, especially the extreme conditions when fire occurs, it provides a more spatially and temporally homogenous long-term dataset of meteorological conditions associated with the life cycle of fire events (Parker et al., 2016).

In this study, we use the hourly output of temperature and specific humidity profiles with 37 pressure levels on a latitude-longitude grid of $0.25^o \times 0.25^o$ from an updated version of ERA5, namely ERA5.1. Both ERA5 and ERA5.1 provide high quality analyses in the troposphere, with ERA5.1 providing a better representation of the upper stratospheric temperature and water vapor compared to ERA5 (Simmons et al., 2020). In this study, ERA5.1 profiles were collocated to SNPP-*CrIS* FOVs using a nearest neighbor approach within a spatial-temporal window of 1-h and 50 km radius.

2.6. Principal component analysis (PCA)

PCA is a multivariate analysis technique that is commonly used to reduce the dimensionality of data (Pearson, 1901; Hotelling, 1933). It has been widely applied to high spectral resolution IR spectra to deal with the large number (L) of spectral channels that are often highly correlated (Huang and Antonelli, 2001; Antonelli et al., 2004). The information contained in the input radiances from L channels will be preserved by finding a set of L_t orthogonal vectors with $L_t < L$, which accounts for the required data variance determined by the science objective of the study. These orthogonal vectors are referred to as principal components (PCs). The eigenvalue λ_i represents the variance explained by the corresponding ith PC.

In this study, PCA is applied to the two months of SNPP-*CrIS* L1B spectra before, during, and after fires in the SWUS and Amazonia regions to quantify the fire-related spectral differences and their correspondence with local temperature, humidity, and trace gas concentration changes. *CrIS* channels that have a quality control (QC) value of 2 ("do not use") are excluded using the QC flags reported in the L1B products. Following Goldberg et al. (2003) and Antonelli et al. (2004), the spectra are normalized by the mean noise equivalent differential radiance to make the noise approximately white before applying PCA, in order to avoid fitting the noise instead of real signal variations. This is especially important for spectral regions where instruments have higher noise or spectral regions containing weak absorption features of trace gases. For comparison purposes and future real-time applications, PCA is also applied directly to the spectra without the noise normalization. The PCs of the covariance matrix of the spectra are then computed.

It is challenging to determine the optimal value of PC numbers (L_t) from real observations that removes the uncorrelated noise while retaining all the meaningful spectral signals. A widely accepted method to determine L_t is to require the ratio between cumulative variance explained by the first L_t PCs to the total data variance to be close to 1 (Jolliffe, 2002) although limitations of this method are noticed (e.g., Antonelli et al., 2004). Here, we use the threshold of total explained data variance to be 99.9%. Following Goldberg et al. (2003), we define mean reconstruction error (REE) for the kth spectrum, $REE_k(L_t)$, and channel-specific reconstruction error for channel i, $REE_i(L_t)$, respectively:

$$REE_k(L_t) = \left[\frac{1}{L}\sum_{i=1}^{L}\left[I_{i,k} - R_{i,k}(L_t)\right]^2\right]^{1/2}$$

$$REE_i(L_t) = \left[\frac{1}{n}\sum_{k=1}^{n}\left[I_{i,k} - R_{i,k}(L_t)\right]^2\right]^{1/2}$$

where L and n are the number of channels and number of spectra in the observations, respectively. $I_{i,k}$ and $R_{i,k}$ are the observed and reconstructed brightness temperatures (BT) at Channel i for the kth spectrum, respectively. The latter are reconstructed using the first L_t eigenvectors.

In the calculation of REE, both the reconstructed and the observed spectra are from the same set of observations, i.e., reference data or training data, thus REE characterizes the errors in PCA fitting. However, if the reference dataset is different from the target dataset, the difference between the reconstructed spectra and the observations indicates differences between the reference and target datasets, which, in our study, are the differences between the two atmospheric states, such as with and without active fire, before and after fire. For simplicity of the discussion, such difference is referred to as reconstruction score, RSC, which has been proven to be an effective measure to detect atmospheric features that are not included in the reference dataset, such as extreme events (Hultberg et al., 2017). In our study, to characterize the spectral differences due to the impact of fire, we use the observations before fires as the reference or training data. The during- and after-fire spectra are then reconstructed using the PCs of before-fire spectra, and the RSCs are then calculated. Since other factors such as regional differences and day-night differences have been excluded by the collocation and case selection method, RSCs characterize the main differences associated with fire between during- ($RSC_{during\text{-}fire}$) or after-fire ($RSC_{after\text{-}fire}$) and before-fire conditions.

3. Results and discussions

3.1. CrIS channel equivalent widths

The high spectral resolution of *CrIS* (as well as its predecessors *AIRS* and *IASI*) enables the sensitivity on the vertical distribution of atmospheric temperature and humidity, and other trace gases, which are important parameters to monitor the local thermodynamic conditions and emissions related to fires (Barnet et al., 2023; Xiong et al., 2022). Fig. 2a shows the locations of the clear-sky weighting function peaks in pressure for each *CrIS* FSR channel based on the 1976 US Standard Atmosphere, calculated using the principal component-based radiative transfer model (PCRTM, Liu et al., 2006) following Hamming apodization.

Fig. 2b shows the *CrIS* channel-based equivalent width, W_ν, for the major absorbers in the IR spectral region to qualitatively demonstrate the gaseous absorption contributions at each *CrIS* channel. The equivalent width is commonly used to characterize molecular abundance in stellar atmospheres based on the area contained within a spectral line at a given wavenumber ν (Rutten, 2003):

$$W_\nu = \left(1 - \frac{B_\nu(T_L)}{B_\nu(T_R)}\right)\int_{line}(1 - e^{-\tau_\nu})d\nu$$

Here, B_ν is the Planck function, T_L and T_R are the temperatures of the absorbing gas and reference background, repectively, and τ_ν is the optical thickness of the line. W_ν is positive for absorption lines and negative for emission lines and has units of frequency (cm^{-1}). Under the weak absorption line assumption, where $e^{-\tau} \approx 1 - \tau$ for absorbing gas species j and line index i, the equivalent width normalized by the thermal contrast at the line center $\nu_{o,ij}$ can be written as:

$$W'_{ij} = \frac{W_{\nu_{0,ij}}}{1 - \frac{B_{\nu_{0,ij}}(T_L)}{B_{\nu_{0,ij}}(T_R)}} = \alpha_{j,i}A_j$$

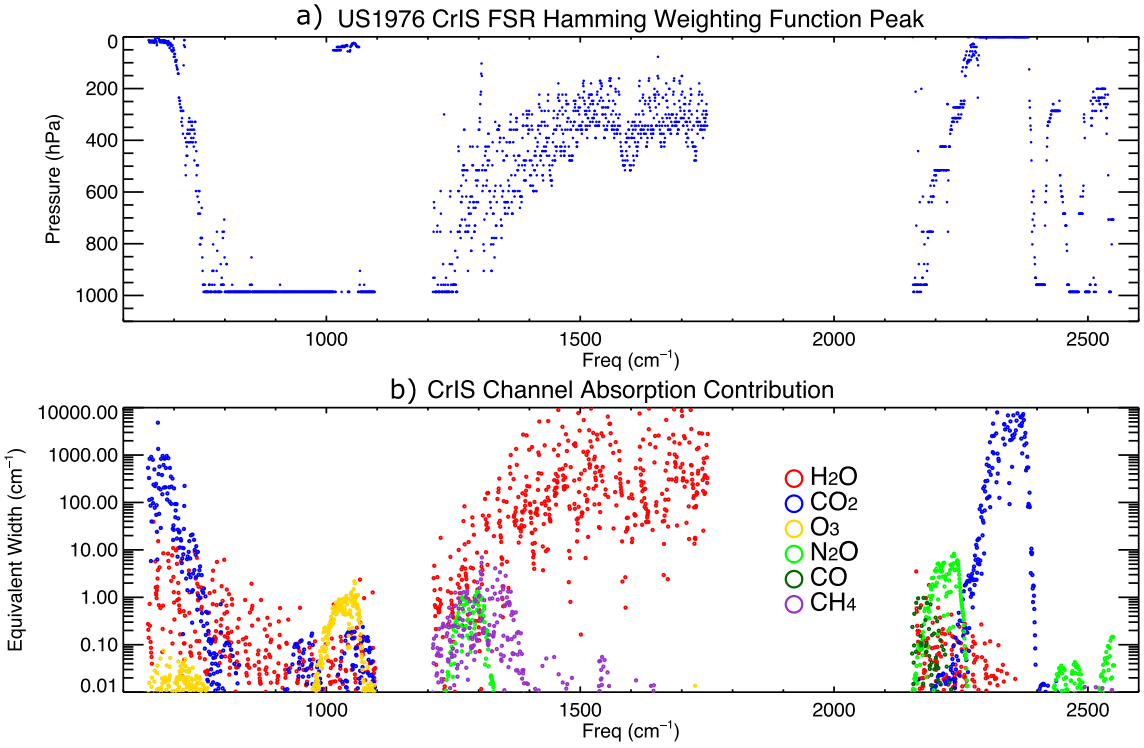

Fig. 2. (a) shows the peak of the clear-sky weighting function in pressure for each *CrIS* FSR channel based on the 1976 US Standard Atmosphere, calculated using the principal component-based radiative transfer model (PCRTM, Liu et al., 2006) following Hamming apodization. (b) shows the *CrIS* channel-based equivalent width for the major absorbers, such as H_2O, CO_2, O_3, N_2O, CO, and CH_4, in the IR spectral region to qualitatively demonstrate the gaseous absorption contributions at each *CrIS* FSR channel.

where $\alpha_{j,i}$ is line strength and A_j is the species abundance. In hyperspectral atmospheric remote sensing, the contribution of the gas species j on channel k with spectral response function $S_k(\nu)$ can be approximated by summarizing the normalized equivalent width over all isotopologues of this gas species and their fractional abundances:

$$W^*_{k,j} = \sum_i S_k(\nu_{0,ij}) W'_{ij}.$$

Although the assumption of weak absorption and linearization of optical depth introduces errors, $W^*_{k,j}$ provides a simple, instrument channel-based approximation characterizing the relative importance of different species to the sensitivity of the IR sounding instrument, as shown in Fig. 2b for SNPP-*CrIS* FSR channels.

The two panels together in Fig. 2 demonstrate the capability of *CrIS* to sound the vertical profiles of the atmosphere. Taking carbon monoxide (CO) as an example, the contribution of CO is seen in the *CrIS*

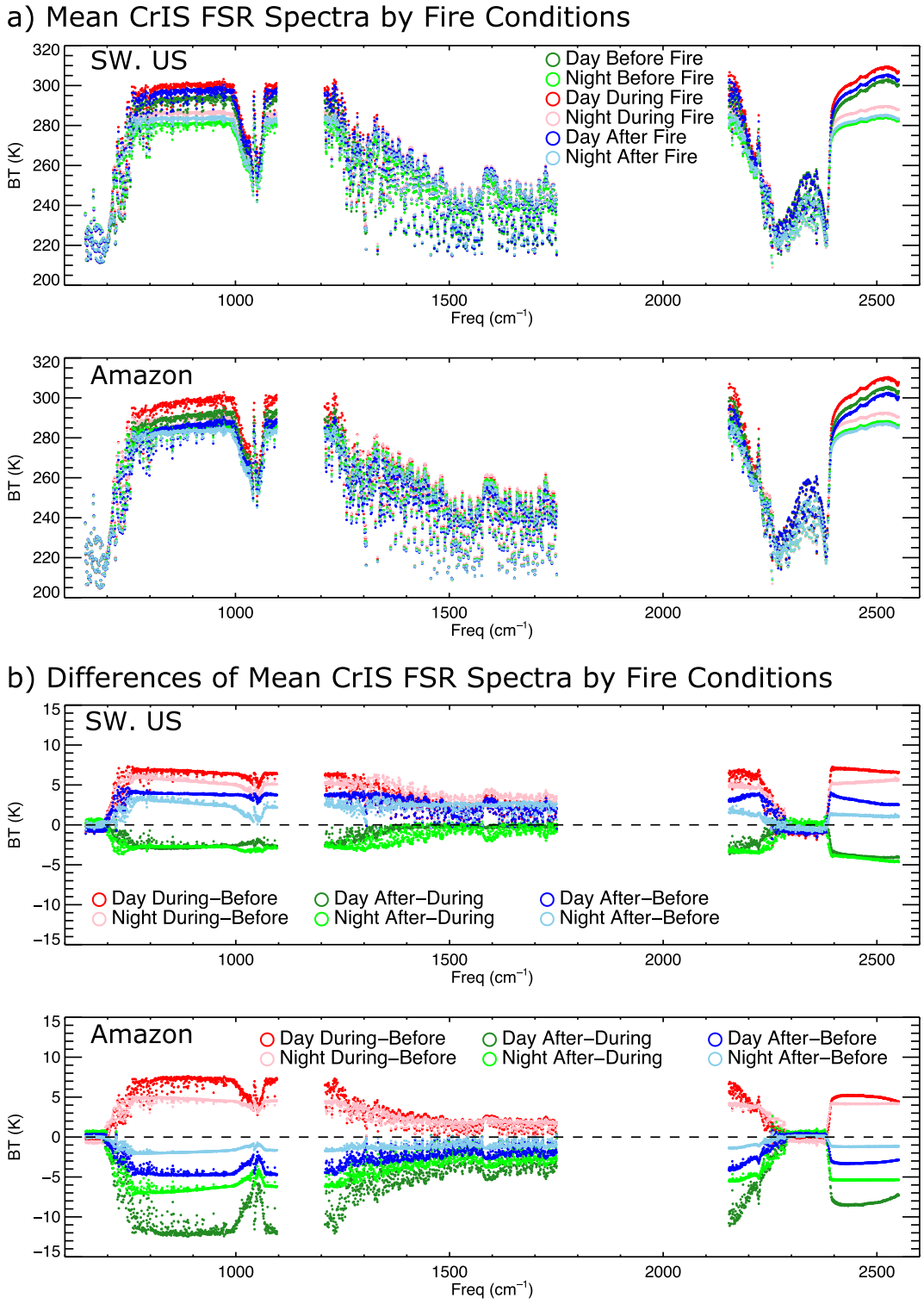

Fig. 3. (a) Mean *CrIS* FSR radiance spectra before, during, and after fires in the two regions for daytime and nighttime conditions; (b) The differences of the *CrIS* mean spectra between different fire conditions for the two regions in daytime and nighttime observations.

channels covering the R-branch of the thermal-IR CO fundamental band above 2155 cm^{-1} (Fig. 2b). CO is formed during biomass burning, by incomplete combustion of biomass and fossil fuel and by oxidation of methane (CH_4) and volatile organic compounds (Worden et al., 2022). For fire events, CO's relatively long lifetime of a few weeks to months in the atmosphere makes it an effective tracer of pollution plumes and their subsequent transport (George et al., 2009). *CrIS* short-wave IR channels in the 4.3 μm CO_2 channels also show high sensitivity to the lower atmospheric temperature. Sensitivity to water vapor profiles is clearly seen in the mid-wave IR channels.

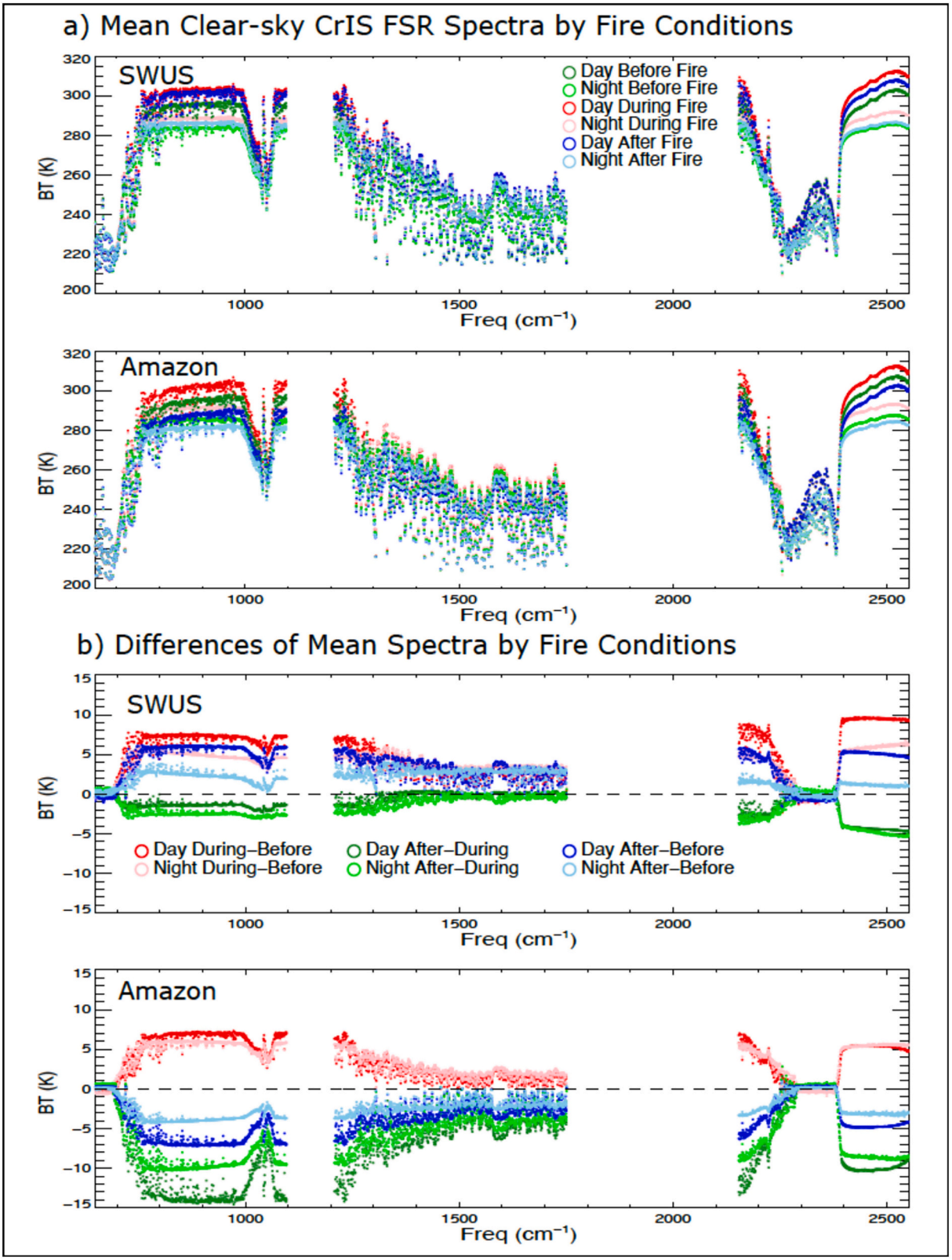

Fig. 4. Similar with Fig. 3 but for clear sky cases only.

3.2. CrIS mean spectra before, during, and after fires

Fig. 3 shows the average *CrIS* BT spectra in the SWUS and Amazonia regions for before-, during-, and after-fire conditions, obtained using the two months of satellite data. The procedure of defining the before-, during-, and after-fire spectra are described in Section 2 and Appendix A. Daytime (dark green, dark red, and dark blue) and nighttime (light green, light red, and light blue) spectra are plotted separately to account for day-night differences due to solar radiation contributions to the SWIR channels and the algorithm differences in *VIIRS* active fire products.

Channels that are sensitive to the surface may be affected by clouds. To further separate the impacts due to clouds, the mean spectra in clear sky conditions are shown in Fig. 4. The IR effective cloud fraction (ECF) as retrieved by the Community Long-Term Infrared Microwave Combined Atmospheric Product System (CLIMCAPS; Smith and Barnet, 2020) for SNPP are used to flag a cloudy spectrum. The ECF is the product of cloud areal fraction and the IR cloud emissivity, the latter of which is assumed to be spectrally flat in the retrieval of ECF (Susskind et al., 2003). Previous studies show that the *CrIS* ECF is generally consistent with the cloud properties such as the cloud frequency and cloud optical depth measured by *VIIRS* in determining the presence of clouds in the scene (e.g. Yue et al., 2022). *CrIS* FOVs with ECF <10% are considered as "clear" and this filter is applied to the spectra that satisfy the selection procedure as described in Sec. 2.4. Table 1 shows the numbers of "clear-sky" spectra for day- and nighttime.

Fig. 5 shows the errors associated with the mean spectra for clear sky: the standard errors (SE) of the mean spectra (Fig. 5a) and the *CrIS* Noise Equivalent Differential Temperature (NEDT, Fig. 5b). The SE is calculated as the standard deviation divided by the square root of the number of spectra, which describes the uncertainty of the mean spectra, i.e., the precision of the mean spectra calculated from our datasets. The SE for clear sky is larger than all sky (not shown) due to the smaller sample sizes. The larger sample size over Amazonia is also the main driver of the smaller SE in this region than SWUS. The NEDT is calculated from the SNPP-*CrIS* L1B NEDN averaged over cases under different conditions and using the corresponding average scene BT by channel. NEDT describes the noise of the spectra. The scene BT is used to account for the scene dependence of NEDT. The NEDT for 270 K scene temperature is also shown as a reference for the during-fire cases because *CrIS* NEDN is highly scene independent (Tobin et al., 2013).

The mean spectra in Figs. 3 and 4 show that the BTs in the surface channels (with clear-sky weighting functions peaking near the surface in Fig. 2a) during the fire are noticeably higher than fire-free conditions in both regions, due to the enhanced surface and lower tropospheric temperature during fire. Fig. 6 shows the mean differences of temperature and water vapor profiles from the collocated ERA5.1 data aggregated in the same way as the *CrIS* spectra. Although more smoothed spatially and temporally, the collocated ERA5.1 vertical profiles show larger near-surface temperature during fire than fire-free conditions in the Amazon regions, while the SWUS region shows colder near-surface temperature during fires than fire-free means. This may be related to larger heterogeneity of meteorological conditions in the mountainous region that is not correctly represented by reanalysis.

In Figs. 3 and 4, in the IR window channels the after-fire mean BTs are higher than the before-fire mean in the SWUS region, however the Amazon region shows colder after-fire BTs than before fire, which is opposite to what is shown by the mean ERA5.1 differences in near-surface temperature. In the Amazon region, the after-fire atmospheric column water vapor is ~20% wetter than the before-fire conditions (Fig. 6). The enhanced water vapor continuum absorption may contribute to the IR window BT differences observed. However, the window channel BT differences could be due to other factors such as the surface emissivity, and aerosol or clouds that are not successfully removed by our cloud filtering method, which makes direct interpretation of mean spectral differences difficult.

The window channels also show larger BTs during fire than before fire; however, the difference between the two is larger in daytime (red) than in nighttime (pink), with the mid-wave IR water vapor channel BT differences larger in nighttime than daytime. This is consistent with the larger magnitude of atmospheric column drying during fire associated with the nighttime fire events as shown by ERA5.1 in the SWUS region (Fig. 6 red and pink curves). Such day-night difference in water vapor concentration is much smaller in the Amazon region, consistent with a smaller day and night difference between during- and before-fire spectra than that in SWUS.

Table 1
The number of "clear-sky" *CrIS* spectra before, during, and after fire conditions in the SWUS and Amazon regions using the two months of data in this study.

	Day-time			Night-time		
	Before Fire	During Fire	After fire	Before Fire	During Fire	After fire
SWUS	461	446	489	76	62	94
Amazonia	7864	8869	7714	1790	1580	2279

3.3. Pixel-scale CrIS spectral sensitivity to collocated VIIRS fire characteristics on selected channels

To further investigate the *CrIS* spectra sensitivity to the fire characteristics at the pixel level, we select two spectral channels: 1231.25 cm^{-1}, a mid-IR window channel, and 2520.00 cm^{-1}, a shortwave IR channel as the water vapor contribution is minimal in this channel using the calculated *CrIS* channel equivalent width. Fig. 7 correlates the *CrIS* BTs from these two channels as a function of the spatial extent and the strength of fire within the FOV. The symbol color represents the *CrIS* FOV total FRP, calculated by summing up the FRP of all collocated *VIIRS* pixels within the *CrIS* FOV. The black and gray circles are the before- and after- fire conditions (both fire-free) within five days at the active fire locations. The symbol size corresponds to the percent of *CrIS* FOV covered by fire as identified by the *VIIRS* 750-m active fire product. The distinctively higher BTs in the 2520 cm^{-1} channel compared to the fire-free conditions demonstrate the sensitivity of *CrIS* to fire events in both day and night-time conditions, with limited signals to smaller fires (symbols with smaller sizes and colder colors). The sensitivity is higher during the night than during the day. In both regions, nighttime fires with above about 200 MWatts (MW) FOV-total FRP are visibly separated from the non-fire scenes; yet during daytime, fires with FOV FRP above about 1000 MW can be separated from the fire-free conditions. In terms of FOV-average FRP that is calculated as the mean *VIIRS* FRP over the collocated *CrIS* FOV, these numbers become 1 MW and 5 MW for day- and nighttime, respectively. The distinction between the fire and fire-free conditions from the two channels is only apparent for fires that occupy >1% of *CrIS* FOVs.

The higher spectral resolution of *CrIS* FSR measurements enables the monitoring of the trace gas emissions associated with fire. The BT difference between the two *CrIS* channels at 2183.12 cm^{-1} and 2185.00 cm^{-1} is shown in Fig. 8 as a function of fire spatial extent (symbol sizes) and FOV-total FRP (colors). The two channels correspond to a strong and a weak CO absorption channel with similar contributions from temperature and humidity. Therefore, their difference is a proxy of the abundance of CO in the atmosphere. A strong correlation between the CO abundance with the FRP of the fires are found in both regions.

3.4. Understanding CrIS spectral sensitivity to fire environment change using the PCA method

Scatterplots like Fig. 7 and Fig. 8 highlight the potential sensitivity of hyperspectral IR measurements to fire characteristics and fire-related local atmospheric states on selected channels. PCA is an effective method to reduce the dimension of the spectral observations while

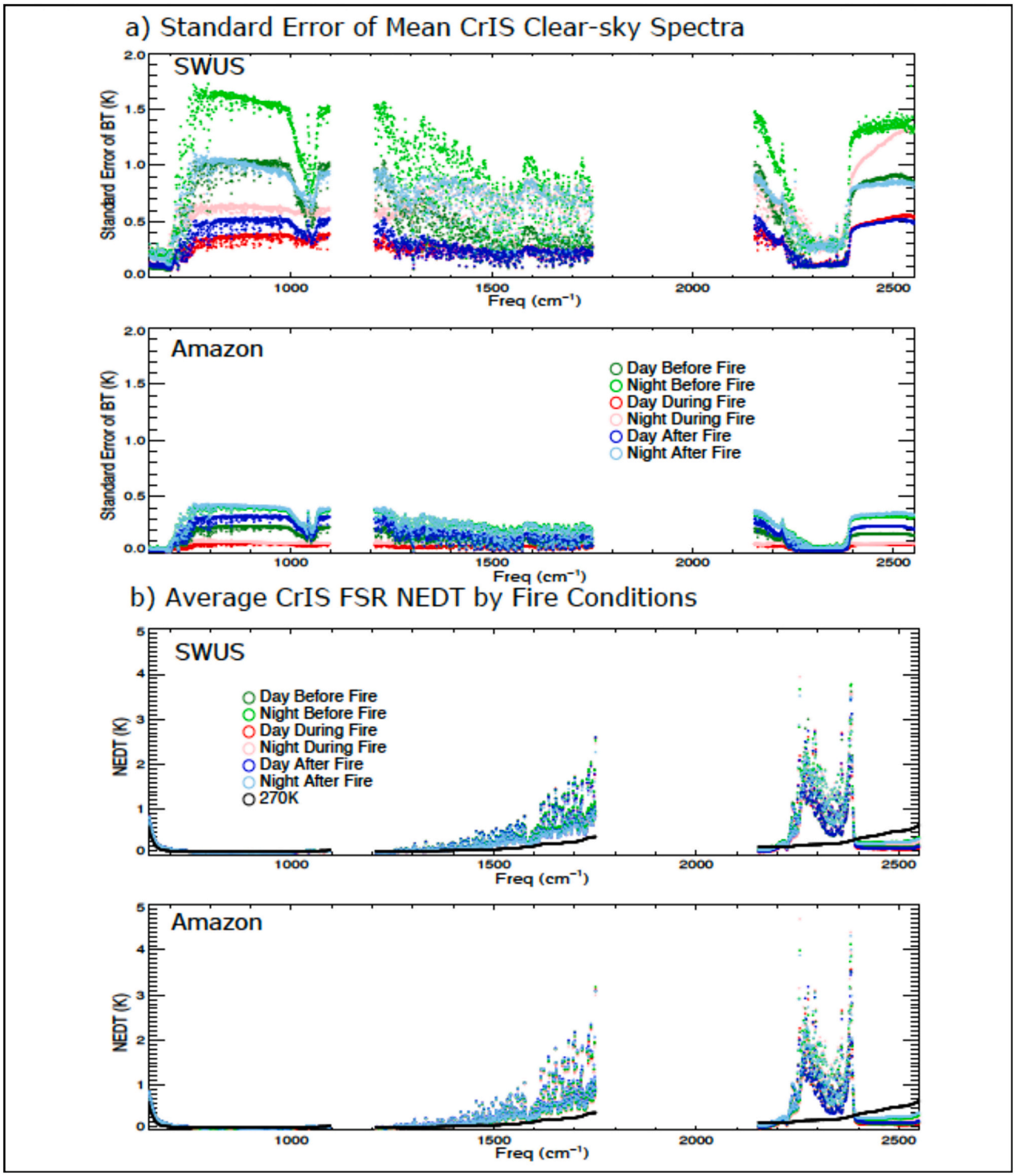

Fig. 5. The standard errors (SE) of the mean clear sky spectra (a) and the *CrIS* Noise Equivalent Differential Temperature (NEDT, b) before, during, and after fires in the two regions for daytime and nighttime conditions as shown by different colors. The SE is calculated as the standard deviation divided by the square root of the number of spectra. The NEDT is calculated from the SNPP-*CrIS* L1B NEDN averaged over cases under different conditions using the corresponding average scene brightness temperature (BT) by channel. The NEDT for 270 K scene temperature is also shown as a reference (black).

retaining the full hyperspectral information from the IR sounders.

Table 2 shows the number of PCs (L_t) needed to explain 99.9% of spectra variance of the noise-normalized spectra and the original *CrIS* spectra before, during, and after fire in the SWUS and Amazonia regions, for which L_t is generally <10. The noise-normalized spectra generally require a slightly smaller L_t. The during-fire spectra L_t values are always larger than their counterpart in fire-free conditions, indicating higher spectral variability during fire. Fig. 9 shows the cumulative variance explained by the first 10 PCs for day- (solid) and night-time (dash) spectra. Darker and lighter colors correspond with SWUS and Amazonia regions, respectively. The variance associated with the leading PCs is smaller using noise-normalized spectra in all conditions, and is

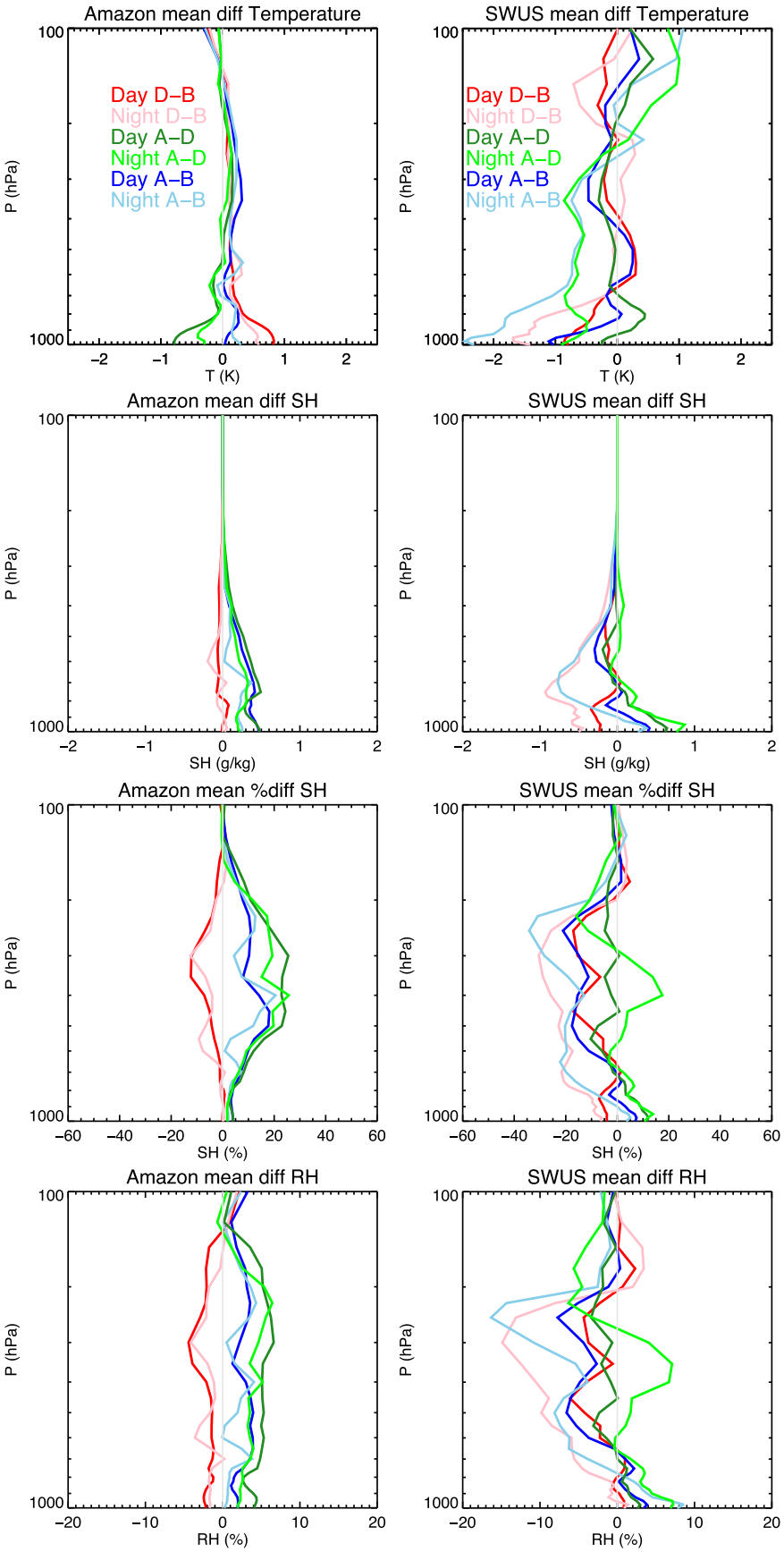

Fig. 6. The differences of SNPP-*CrIS* collocated ERA5 temperature and water vapor vertical profiles between different fire conditions over Amazonia (left) and the SWUS (right). From top to bottom are the temperature (T in K), specific humidity (SH in g kg^{-1}), specific humidity difference relative to the minuend (%), and the relative humidity (RH in %).

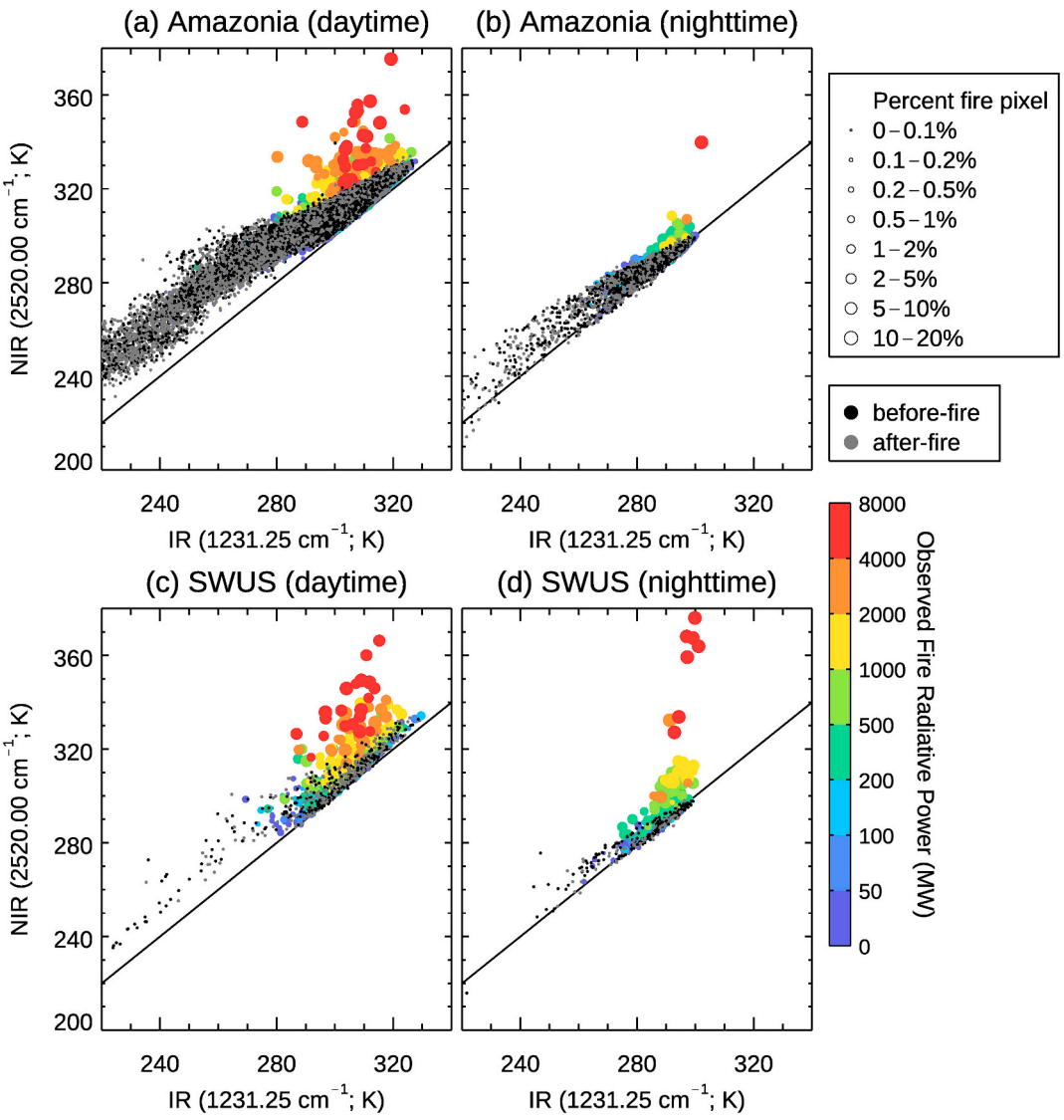

Fig. 7. The *CrIS* spectral sensitivity to the fire characteristics at the pixel level. The scatterplot shows the correlation between the brightness temperatures at two spectral channels: 1231.25 cm^{-1}, a mid-IR window channel, and 2520.00 cm^{-1}, a shortwave IR channel as the water vapor contribution is minimal in this channel. The symbol color represents the total *CrIS*FRP over each *CrIS* FOV, calculated as the sum of the FRP of all collocated *VIIRS* pixels within the *CrIS* FOV. The black and gray circles are the before and after fire conditions (fire-free) within five days at the active fire locations. The symbol size corresponds to the percent of *CrIS* FOV covered by fire as identified by the *VIIRS* 750-m active fire product. Daytime and nighttime observations in Amazon and SWUS regions are shown in different panels.

decreasing from before fire, after fire, to during fire conditions with larger values from the day- than night-time observations. These values of L_t are much smaller compared to other studies applying PCA to *CrIS*-like hyperspectral IR spectra. Using the simulated AIRS all-sky radiances, Goldberg et al. (2003) showed that <10 PCs could explain nearly 100% of the variance and ~ 60 PCs are needed to reconstruct the AIRS spectra within the instrument noise level. They further recommended to keep the 200 PCs to assure sufficient information is saved to reconstruct the AIRS radiances. Atkinson et al. (2008) derived 150 PCs using approximately 16,000 spectra from 6 months of thinned IASI data. In a subsequent study, Atkinson et al. (2010) selected around 300 PCs from a global sample of about 75,000 IASI spectra plus approximately 6600 cases associated with fire and volcano eruption. Barnet et al. (2023) use approximately 100 PCs to perform full-on IR retrievals from *CrIS* FSR radiances with the number of PCs locally determined for each individual spectrum.

The smaller values of L_t in this study are attributed to the fact that our datasets are specifically associated with active fire events and their immediately before- and after-fire conditions within two months in a particular region. Consequently, the range of variance represented by our dataset is much narrower than the global all-condition analyses reported in other studies. Additionally, the small sample sizes (592 day- and 150 night-time *CrIS* FOVs in the SWUS region; 14,672 day- and 3647 night-time FOVs in Amazonia) also contribute to the limited number of leading PCs (Jolliffe, 2002; Antonelli et al., 2004). Nonetheless, these results highlight the distinctive spectral signature of *CrIS* radiances related to fire and associated environmental changes, demonstrating the benefit of PCA.

Figs. 10 and 11 show both the REE (dashed lines) and RSC (dots) calculated using the first 50 PCs for the two regions, respectively. Overlain are the weighting function peaks and *CrIS* channel specific equivalent width for the major IR absorbers shown in Fig. 2. The small REE values demonstrate the application of PCA to reduce the data volume while retaining the information of spectra under different conditions. As discussed in Section 2.5, RSCs with magnitudes larger than reconstruction error and measurement error show the distinctive spectral features in the target dataset (spectra during and after-fire) that are not included in reference or training set (before-fire spectra). The

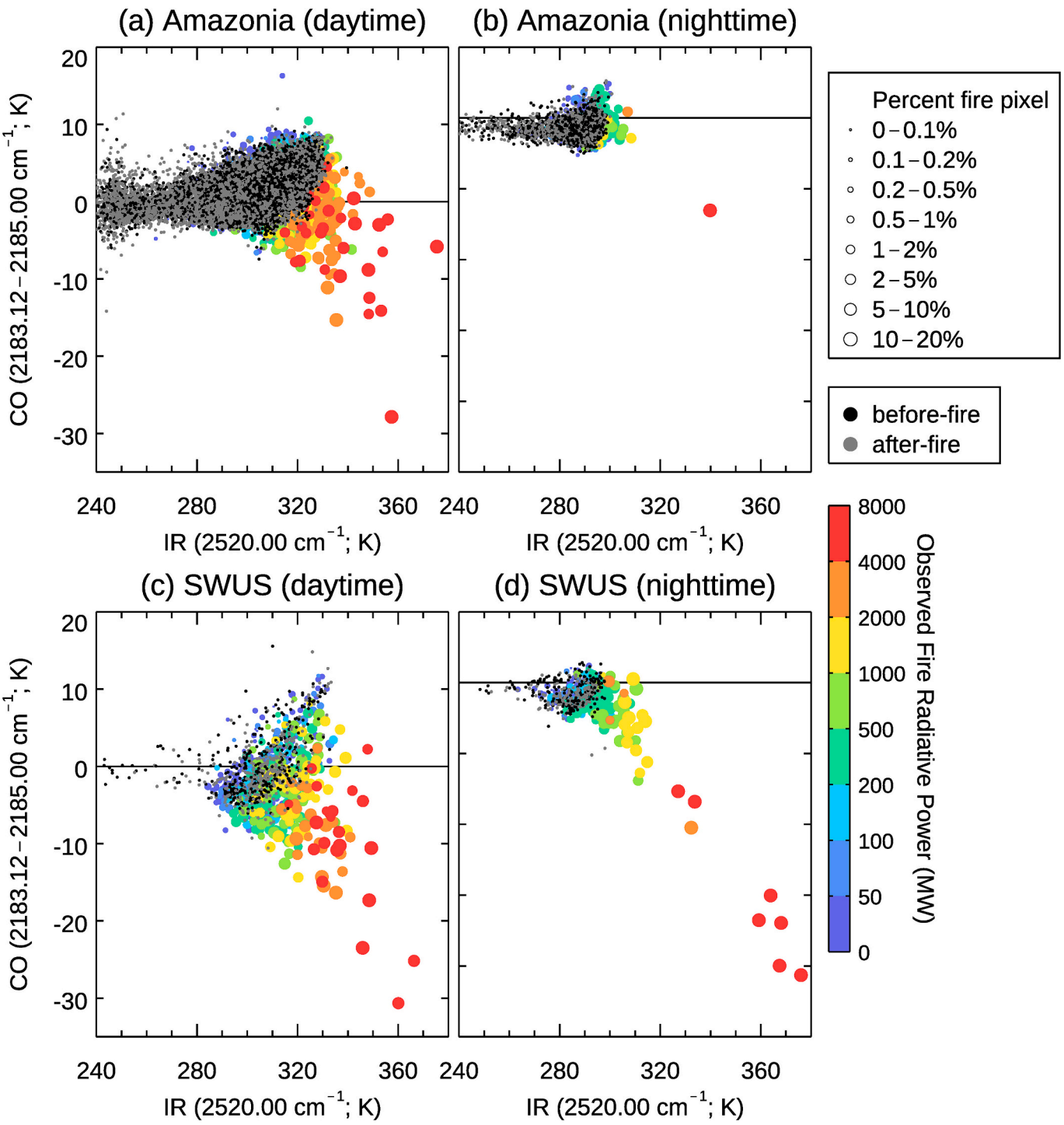

Fig. 8. The sensitivity of *CrIS* CO plume to the size and strength of the fire, shown by the BT differences between the two *CrIS* FSR channels located at 2183.12 and 2185.00 cm^{-1} as functions of fire spatial extent (symbol size) and FOV total FRP (symbol color). The two channels correspond to a strong and a weak CO absorption channel with similar contributions from temperature and humidity.

differences in the shortwave IR channels, CO absorption bands, and the CO_2 4.3 μm bands are apparent. The strong signals as shown by large RSCs are also seen in the mid-wave IR water vapor sounding channels ~1250 cm^{-1}, whose weighting functions peak in the lower troposphere (Barnet et al., 2023; Pan and Huang, 2018). This indicates changes in lower troposphere humidity between before and after fire that could be retrieved from the *CrIS* observations. These results highlight the potential of efficiently detecting fire-induced local atmospheric condition changes from the *CrIS* FSR observations using the PCA method. The collocated sounder and imager data thus can provide the training data that are necessary for such application and train algorithms to detect and retrieve emissions and thermodynamic environmental changes due to fire.

4. Concluding remarks

This study analyzed the infrared (IR) spectral signature of wildfires and the IR sounder instrumental sensitivity to size and strength of fire

Table 2
The number of PCs (L_t) needed to explain 99.9% of spectra variance of the noise-normalized and original *CrIS* spectra before, during, and after fire conditions in the W. US and Amazonia regions using the two months of data in this study.

	Day-time L_t from noise normalized (and original) *CrIS* spectra			Night-time L_t from noise normalized (and original) *CrIS* spectra		
	Before Fire	During Fire	After fire	Before Fire	During Fire	After fire
SWUS	5 (6)	8 (10)	6 (7)	5 (5)	9 (10)	6 (7)
Amazonia	4 (5)	7 (9)	3 (5)	5 (5)	11 (12)	4 (4)

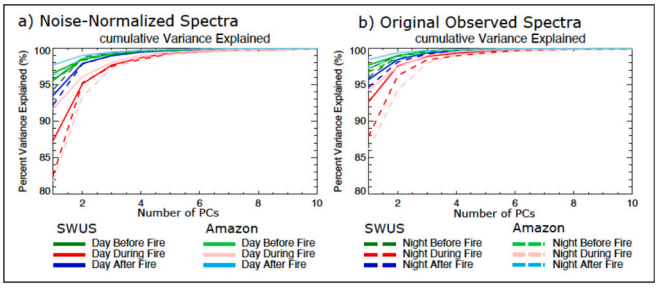

Fig. 9. The cumulated variance explained for the first 10 PCs of the noise-normalized *CrIS* spectra (a), and original *CrIS* spectra (b) for different composites during the day and night time for SWUS and Amazon regions.

events using a pixel-scale collocated product between the space-borne sounders and imagers. Leveraging the strengths of both instruments allows for detailed quantitative analysis of the spectral characteristics of sounders associated with high-spatial fire properties measured by imagers, encompassing the stages of before, during, and after fires.

Using two months of collocated SNPP-*CrIS* and *VIIRS* observations in two selected regions (SWUS, and Amazonia), we found that *CrIS* displays high sensitivity to fires that affects as little as 1% of its FOV with total FRP larger than 200 MW at night and 1000 MW during the day in the *CrIS* FOV. Similar dependence of *CrIS* CO signals to the size and strength of the fire is shown using the BT difference between two *CrIS* channels (2183.12 and 2185.00 cm^{-1}, which are 4.581 and 4.577 μm in wavelength, respectively) as a proxy.

To better understand the spectral signature of fire and the fire atmospheric states, the PCA method is applied to spectra obtained before, during, and after fire in these two regions. Generally, fewer than 10 leading PCs are needed to account for 99.9% of the spectral variance for all conditions, demonstrating the value of PCA in reducing the data volume while retaining all spectral information, which is key in the application of hyperspectral sounding observations. Using before-fire spectra as the training dataset, a method to efficiently identify fire and the atmospheric state differences related to fire is shown using the reconstruction score (RSC) of PCA. The magnitude of RSC is much larger than that of PCA fitting errors as shown by the reconstruction errors (REE). The large differences in RSCs between the after- and during-fire spectra relative to the before-fire spectra illustrate the spectral signal of fire, and the atmospheric temperature, CO, and lower tropospheric humidity changes caused by fire. Therefore, the collocated imager fire and IR sounder radiance observations could be used to build training datasets for applications which use machine learning methods to detect and monitor extreme events like fire. Our study could be extended to the multi-decadal observations records of synergistic sounder and imager measurements from multiple satellites, which will build long-term data records to study the interactions between fire and the climate system. This could benefit from the efforts to develop the PCA based L1B products for space-borne hyperspectral IR sounders, such as the *IASI* PCA-based products (EUMETSAT, 2022) and the newly released *CrIS* L1B PCA / Rapid Event Detection products (https://disc.gsfc.nasa.gov/datacollection/SNDRJ1CrISL1BPCARED_3.0.html).

Recently, the NASA FireSense program selected the Pyro-atmosphere InfraRed Sounder (PIRS) instrument. PIRS measures the shortwave IR spectral region with a much higher spatial resolution, aiming to provide

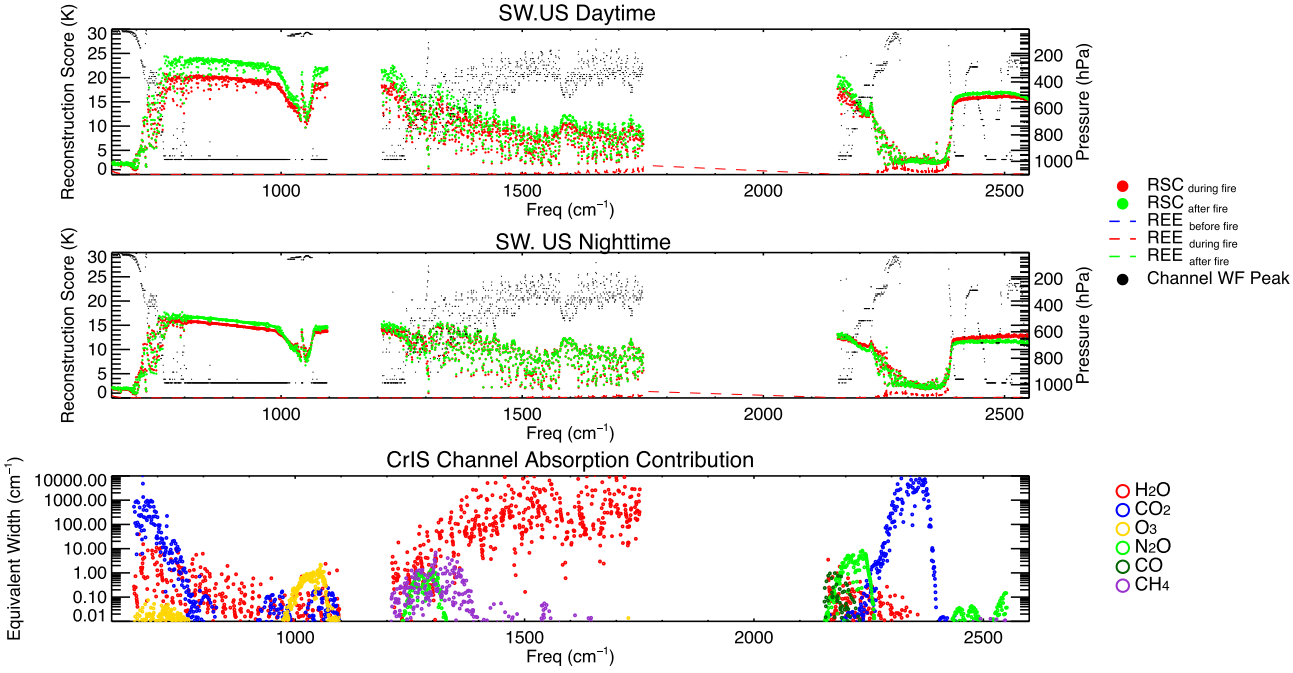

Fig. 10. Channel-specific REE and RSCs for spectra in the SWUS regions for day- (upper) and night-time (middle) *CrIS* observations in the SWUS region. Dashed lines show the channel-specific REEs for *CrIS* spectra in the before-, during-, and after-fire conditions using the first 50 PCs. Colored dots show the RSC for during-fire spectra (red), and after-fire (green) spectra that are calculated using the first 50 PCs of the before-fire spectra, respectively. Overlain are the weighting function peaks and *CrIS* channel specific equivalent width for the major IR absorbers (bottom) shown in Fig. 2. (For interpretation of the references to color in this figure legend, the reader is referred to the web version of this article.)

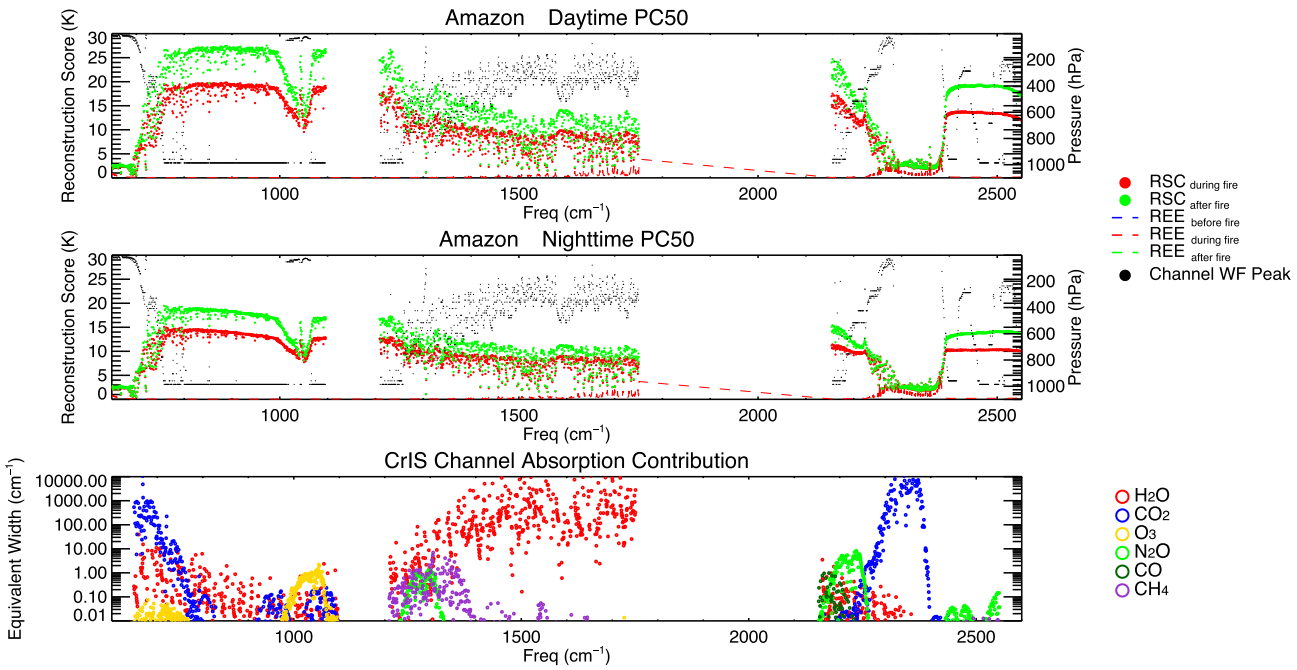

Fig. 11. Same as Fig. 10 except for the Amazonia.

3-dimensional information about the state of the atmosphere during the pre- and active-fire stages of wildland fires. The method developed here could benefit the onboard data processing and potential retrieval algorithm development for PIRS and other IR sounding instruments.

CRediT authorship contribution statement

Xuyang Zhou: Writing – original draft, Software, Formal analysis. **Qing Yue:** Writing – review & editing, Writing – original draft, Visualization, Validation, Supervision, Software, Resources, Project administration, Methodology, Investigation, Funding acquisition, Formal analysis, Data curation, Conceptualization. **King-Fai Li:** Writing – review & editing, Visualization, Formal analysis, Data curation. **Evan Fishbein:** Writing – review & editing, Software, Data curation. **Xiuhong Chen:** Writing – review & editing, Software, Data curation. **Lin Tan:** Writing – review & editing. **Sally Newman:** Writing – review & editing. **Eric Fetzer:** Funding acquisition, Data curation. **Yuk L. Yung:** Writing – review & editing, Resources, Project administration.

Declaration of competing interest

The authors declare that they have no conflict of interest.

Data and code availability

VIIRS/NPP Thermal Anomalies/Fire 6-Min L2 Swath 750 m V001 was obtained from NASA EOSDIS Land Processes Distributed Active Archive Center (https://doi.org/10.5067/VIIRS/VNP14.001).

SNPP-*CrIS* Level 1B Full Spectral Resolution V3 (SNPP*CrIS*L1B) data was obtained from the NASA Goddard Earth Sciences Data Information and Services Center (GESDISC) (https://doi.org/10.5067/ZCRSHBM5HB23).

SNPP *CrIS-VIIRS* 750-m Matchup Indexes V1 (SNPP_*CrIS_VIIRS*750-m_IND) was obtained from NASA GESDISC (https://doi.org/10.5067/MEASURES/WVCC/DATA211).

SNPP-CrIS effective cloud fraction data was obtained from the Sounder SIPS SNPP CLIMCAPS Full Spectral Resolution Version 2 Level 2 Atmosphere cloud and surface geophysical state retrieval products at GESDISC (https://doi.org/10.5067/62SPJFQW5Q9B).

Acknowledgements

The research was carried out at the Jet Propulsion Laboratory, California Institute of Technology, under a contract with the National Aeronautics and Space Administration (80NM0018D0004). XZ and QY were supported by the NASA Decadal Survey Incubator program. QY was also supported by NASA's Making Earth Science Data Records for Use in Research Environments (MEaSUREs) program. QY and EF acknowledge the support of the *AIRS* Project at JPL and the sounder SIPS at JPL. LT was partially supporting by the UC Riverside Central Fellowship for Graduate Studies. YLY acknowledge support from the Anna Tai foundation to Caltech.

Appendix A. Collocating VPN14 L2 and SNPP-*CrIS* L1b FSR products using the SNPP *CrIS–VIIRS* 750-m Matchup Indexes for before, during, and after fire conditions

The data products used in this study and their codenames are summarized in Table A1. One SNPP_*CrIS_VIIRS*750m_IND file contains data for one *CrIS* granule, which gives the matchup indices of SNPP-*VIIRS* pixels within each SNPP-*CrIS* FOV. Due to small spatio-temporal mismatch between the granulizations of the two sensors, each SNPP-*CrIS* L1B FSR file could overlap with up to three SNPP-*VIIRS* granules. The granule IDs are provided in the matchup index files for VNP03MOD products, which are used to find the corresponding VNP14 files. These VNP14 files are then concatenated in the temporal order (along-track direction).

Table A1
The data files used in this study. {T} stands for the acquisition time. {G} stands for the granule number. {P} stands for the processing time. {V} is either "VPN14" or "VNP03MOD".

Data Products	Filenames
VNP14 or VNP03MOD	{V}.A{T}0.001.{P}.nc
CrIS FSR L1B	SNDR.SNPP.*CRIS*.{T}.m06.{G}.L1B.std.v03_08.G.{P}.nc
SNPP_*CrIS_VIIRS*750m_IND	IND_*CrIS_VIIRS*MOD_SNDR.SNPP.{T}.g{G}.nc

Each SNPP_*CrIS_VIIRS*750m_IND file has a 45 along-track×30 cross-track×9 FOV array, named FOVCount_ImagerPixel, which specifies the number of *VIIRS* pixels in each *CrIS* FOV. Where FOVCount_ImagerPixel is non-zero, the along-track (named number_of_pixels) and cross-track (named number_of_lines) indices of the SNPP-*VIIRS* pixels (after concatenation) in different *CrIS* FOVs are stored serially in temporal order. If a pair of the SNPP-*VIIRS* along-track and cross-track indices in the SNPP_*CrIS_VIIRS*750m_IND file also appears in the concatenated VNP14 indices, then the corresponding *CrIS* FOV is deemed to contain fire, and its spectrum is collected. This way the during-fire *CrIS* spectra and their associated fire characteristics can be obtained.

Fig. A1 shows an example of the collocated VNP14 "during-fire" pixels with the SNPP-*CrIS* FOVs. Once a during-fire spectrum is obtained, the corresponding before-fire spectrum is obtained by repeating the same fire-searching algorithm to the first day prior to the during-fire spectrum except the target now is a non-fire SNPP-*CrIS* FOV (i.e. none of the overlapped *VIIRS* pixels has fire) at the same location. If the during-fire spectrum is a daytime (local standard solar time from 8 AM to 4 PM) spectrum, then the before-fire spectrum must also be a daytime spectrum; similarly, if the during-fire spectrum is a nighttime (local standard solar time from 8 PM to 4 AM) spectrum, then the before-fire spectrum must also be a nighttime spectrum. If the SNPP-*CrIS* FOV one day prior also contains fires, then we search again on the second day prior to the during-fire spectrum, and so on until we have searched through all five days prior to the during-fire spectrum for the first fire-free SNPP-*CrIS* FOV at the same location. The after-fire spectrum corresponding to the during-fire spectrum is obtained in the same way except for the earliest fire-free spectra within five days after the fire events.

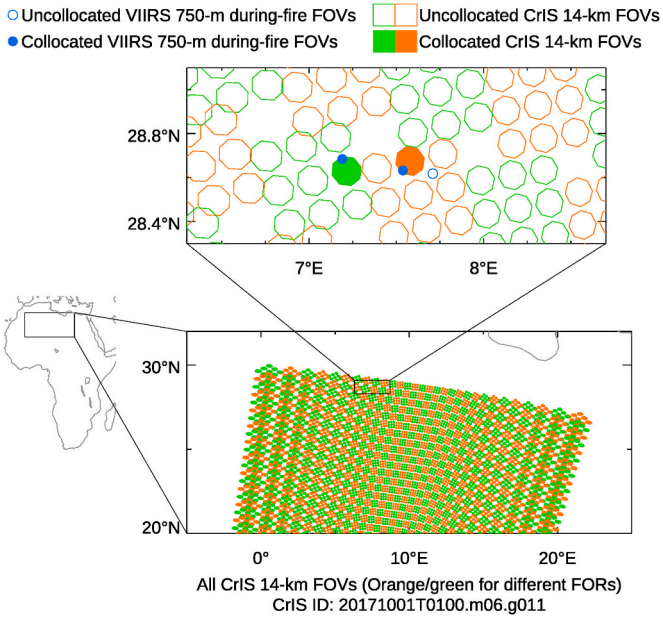

Fig. A1. (Bottom) The field of views (FOVs) of SNPP-CrIS in the 11th granule at 01:00 UTC on October 1, 2017. Each field of regard of *CrIS* consists of a 3×3 array of FOVs. Different FORs are colored by consecutive orange and green. (Top) A zoom-in of the SNPP-*CrIS* granule where two collocated SNPP-*VIIRS* during-fire FOVs (filled circles) over the SNPP-*CrIS* FOVs (filled octagons) are identified. Uncollocated FOVs are shown in open symbols. The octagon boundaries of the *CrIS* FOVs extracted from the FSR product are drawn to the real scale (~14 km in diameter). The circles of the *VIIRS* FOVs in the top panel are not drawn to the real scale. Note the bowtie effects of the SNPP-*CrIS* FOVs at the east/west wings.

References

Abatzoglou, J.T., Williams, A.P., Barbero, R., 2019. Global emergence of anthropogenic climate change in fire weather indices. Geophys. Res. Lett. 46 (1), 326–336. https://doi.org/10.1029/2018GL080959.

Abram, N.J., Henley, B.J., Sen Gupta, A., Lippmann, T.J.R., Clarke, H., Dowdy, A.J., Sharples, J.J., Nolan, R.H., Zhang, T., Wooster, M.J., Wurtzel, J.B., Meissner, K.J., Pitman, A.J., Ukkola, A.M., Murphy, B.P., Tapper, N.J., Boer, M.M., 2021. Connections of climate change and variability to large and extreme forest fires in southeast Australia. Commun. Earth Environ. 2 (1), 8. https://doi.org/10.1038/s43247-020-00065-8.

Andela, N., Morton, D.C., Giglio, L., Paugam, R., Chen, Y., Hantson, S., van der Werf, G. R., Randerson, J.T., 2019. The global fire atlas of individual fire size, duration, speed and direction. Earth System Sci. Data 11 (2), 529–552. https://doi.org/10.5194/essd-11-529-2019.

Antonelli, P., Revercomb, H.E., Sromovsky, L.A., Smith, W.L., Knuteson, R.O., Tobin, D. C., Garcia, R.K., Howell, H.B., Huang, H.-L., Best, F.A., 2004. A principal component noise filter for high spectral resolution infrared measurements. J. Geophys. Res. Atmos. 109 (D23) https://doi.org/10.1029/2004JD004862, 2004JD004862.

Atkinson, N.C., Brunel, P., Marguinaud, P., Labrot, T., 2008. AAPP developments and experiences with processing METOP data. In: Tech. Proc. 16th Int. TOVS Study Conf., Angra dos Reis, Brazil, 6–13 May, 2008.

Atkinson, N.C., Hilton, F.I., Illingworth, S.M., Eyre, J.R., Hultberg, T., 2010. Potential for the use of reconstructed IASI radiances in the detection of atmospheric trace gases. Atmos. Meas. Tech. 3 (4), 991–1003. https://doi.org/10.5194/amt-3-991-2010.

Barnet, C.D., Smith, N., Ide, K., Garrett, K., Jones, E., 2023. Evaluating the value of *CrIS* shortwave-infrared channels in atmospheric-sounding retrievals. Remote Sens. (Basel) 15 (3), 547. https://doi.org/10.3390/rs15030547.

Bowman, D.M.J.S., Williamson, G.J., Abatzoglou, J.T., Kolden, C.A., Cochrane, M.A., Smith, A.M.S., 2017. Human exposure and sensitivity to globally extreme wildfire

events. Nature Ecology Evolution 1 (3), 0058. https://doi.org/10.1038/s41559-016-0058.
Chuvieco, E., Martin, M.P., 1994. Global fire mapping and fire danger estimation using AVHRR image. Photogramm. Eng. Remote Sensing 60 (5), 563–570.
Dickinson, M.B., Hudak, A.T., Zajkowski, T., Loudermilk, E.L., Schroeder, W., Ellison, L., Kremens, R.L., Holley, W., Martinez, O., Paxton, A., Bright, B.C., O'Brien, J.J., Hornsby, B., Ichoku, C., Faulring, J., Gerace, A., Peterson, D., Mauceri, J., 2016. Measuring radiant emissions from entire prescribed fires with ground, airborne and satellite sensors – RxCADRE 2012. Int. J. Wildland Fire 25 (1), 48. https://doi.org/10.1071/WF15090.
EUMETSAT, 2022. IASI principal components scores fundamental data record release 1 - Metop-A and -B. In: European Organisation for the Exploitation of Meteorological Satellites. https://doi.org/10.15770/EUM_SEC_CLM_0084.
Farahmand, A., Stavros, E.N., Reager, J.T., Behrangi, A., 2020. Introducing spatially distributed fire danger from earth observations (FDEO) using satellite-based data in the contiguous United States. Remote Sens. (Basel) 12 (8), 1252. https://doi.org/10.3390/rs12081252.
Fetzer, E., Yue, Q., Manipon, G., Wang, L., 2022. SNPP *CrIS-VIIRS* 750-m Matchup Indexes V1 [Data set]. NASA Goddard Earth Sciences Data and Information Services Center. Accessed: 06/06/2023. https://doi.org/10.5067/MEASURES/WVCC/DATA211.
Field, R.D., Spessa, A.C., Aziz, N.A., Camia, A., Cantin, A., Carr, R., de Groot, W.J., Dowdy, A.J., Flannigan, M.D., Manomaiphiboon, K., Pappenberger, F., Tanpipat, V., Wang, X., 2015. Development of a global fire weather database. Natural Hazards Earth System Sci. 15 (6), 1407–1423. https://doi.org/10.5194/nhess-15-1407-2015.
Flannigan, M.D., Krawchuk, M.A., de Groot, W.J., Wotton, B.M., Gowman, L.M., 2009. Implications of changing climate for global wildland fire. Int. J. Wildland Fire 18 (5), 483. https://doi.org/10.1071/WF08187.
Flannigan, M.D., Wotton, B.M., Marshall, G.A., de Groot, W.J., Johnston, J., Jurko, N., Cantin, A.S., 2016. Fuel moisture sensitivity to temperature and precipitation: climate change implications. Clim. Change 134 (1–2), 59–71. https://doi.org/10.1007/s10584-015-1521-0.
Flasse, S.P., Ceccato, P., 1996. A contextual algorithm for AVHRR fire detection. Int. J. Remote Sensing 17 (2), 419–424. https://doi.org/10.1080/01431169608949018.
George, M., Clerbaux, C., Hurtmans, D., Turquety, S., Coheur, P.-F., Pommier, M., Hadji-Lazaro, J., Edwards, D.P., Worden, H., Luo, M., Rinsland, C., McMillan, W., 2009. Carbon monoxide distributions from the IASI/METOP mission: evaluation with other space-borne remote sensors. Atmos. Chem. Phys. 9 (21), 8317–8330. https://doi.org/10.5194/acp-9-8317-2009.
Giglio, L., Descloitres, J., Justice, C.O., Kaufman, Y.J., 2003. An enhanced contextual fire detection algorithm for *MODIS*. Remote Sensing Environ. 87 (2–3), 273–282. https://doi.org/10.1016/S0034-4257(03)00184-6.
Giglio, L., Schroeder, W., Justice, C.O., 2016. The collection 6 *MODIS* active fire detection algorithm and fire products. Remote Sensing Environ. 178, 31–41. https://doi.org/10.1016/j.rse.2016.02.054.
Goldberg, M.D., Yanni, Qu, McMillin, L.M., Wolf, W., Zhou, Lihang, Divakarla, M., 2003. *AIRS* near-real-time products and algorithms in support of operational numerical weather prediction. IEEE Trans. Geosci. Remote Sensing 41 (2), 379–389. https://doi.org/10.1109/TGRS.2002.808307.
Han, Y., Revercomb, H., Cromp, M., Gu, D., Johnson, D., Mooney, D., Scott, D., Strow, L., Bingham, G., Borg, L., Chen, Y., DeSlover, D., Esplin, M., Hagan, D., Jin, X., Knuteson, R., Motteler, H., Predina, J., Suwinski, L., Taylor, J., Tobin, D., Tremblay, D., Wang, C., Wang, L., Wang, L., Zavyalov, V., 2013. Suomi NPP *CrIS* measurements, sensor data record algorithm, calibration and validation activities, and record data quality. J. Geophys. Res. Atmos. 118 (22) https://doi.org/10.1002/2013JD020344.
Hennermann, K., Berrisford, P., 2020. Era5: Data description. Copernicus Knowledge Base.
Hersbach, H., Bell, B., Berrisford, P., Horányi, A., Muñoz-Sabater, J., Nicolas, J., Radu, R., Schepers, D., Simmons, A., Soci, C., Dee, D., 2019. Global reanalysis: goodbye ERA-Interim, hello ERA5. In: ECMWF Newsletter No. 159. https://www.ecmwf.int/en/newsletter/159/meteorology/global-reanalysis-goodbye-era-interim-hello-era5.
Hersbach, H., Bell, B., Berrisford, P., Hirahara, S., Horányi, A., Muñoz-Sabater, J., Nicolas, J., Peubey, C., Radu, R., Schepers, D., Simmons, A., Soci, C., Abdalla, S., Abellan, X., Balsamo, G., Bechtold, P., Biavati, G., Bidlot, J., Bonavita, M., De Chiara, G., Dahlgren, P., Dee, D., Diamantakis, M., Dragani, R., Flemming, J., Forbes, R., Fuentes, M., Geer, A., Haimberger, L., Healy, S., Hogan, R.J., Hólm, E., Janisková, M., Keeley, S., Laloyaux, P., Lopez, P., Lupu, C., Radnoti, G., De Rosnay, P., Rozum, I., Vamborg, F., Villaume, S., Thépaut, J., 2020. The ERA5 global reanalysis. Quart. J. Roy. Meteorol. Soc. 146 (730), 1999–2049. https://doi.org/10.1002/qj.3803.
Hotelling, H., 1933. Analysis of a complex of statistical variables into principal components. J. Educational Psychol. 24 (6), 417–441. https://doi.org/10.1037/h0071325.
Huang, H.-L., Antonelli, P., 2001. Application of principal component analysis to high-resolution infrared measurement compression and retrieval. J. Appl. Meteorol. 40 (3), 365–388. https://doi.org/10.1175/1520-0450(2001)040<0365:AOPCAT>2.0.CO;2.
Hultberg, T.H., August, T., Lenti, F., 2017. Local or global? How to choose the training set for principal component compression of hyperspectral satellite measurements: A hybrid approach. In: Meynart, R., Neeck, S.P., Shimoda, H., Kimura, T., Bézy, J.-L. (Eds.), Sensors, Systems, and Next-Generation Satellites XXI. SPIE, Warsaw, Poland, p. 50. https://doi.org/10.1117/12.2278349.
Jain, P., Castellanos-Acuna, D., Coogan, S.C.P., Abatzoglou, J.T., Flannigan, M.D., 2022. Observed increases in extreme fire weather driven by atmospheric humidity and temperature. Nat. Clim. Chang. 12 (1), 63–70. https://doi.org/10.1038/s41558-021-01224-1.
Jiang, X., Li, K., Liang, M., Yung, Y.L., 2021. Impact of Amazonian fires on atmospheric CO2. Geophys. Res. Lett. 48 (5) https://doi.org/10.1029/2020GL091875 e2020GL091875.
Jolliffe, I.T., 2002. Principal Component Analysis, 2nd ed. Springer, New York.
Jones, M.W., Abatzoglou, J.T., Veraverbeke, S., Andela, N., Lasslop, G., Forkel, M., Smith, A.J.P., Burton, C., Betts, R.A., van der Werf, G.R., Sitch, S., Canadell, J.G., Santín, C., Kolden, C., Doerr, S.H., Le Quéré, C., 2022. Global and regional trends and drivers of fire under climate change. Rev. Geophys. 60 (3) https://doi.org/10.1029/2020RG000726 e2020RG000726.
Kaufman, Y., Remer, L., Ottmar, R., Ward, D., Rong-R, L., Kleidman, R., Fraser, R., Flynn, L., McDougal, D., Shelton, G., 1996. Relation-ship between remotely sensed fire intensity and rate of emission ofsmoke: SCAR-C experiment. In: Levine, J. (Ed.), Global Biomass Burning. MIT Press, MA, pp. 685–696.
Kelley, D.I., Bistinas, I., Whitley, R., Burton, C., Marthews, T.R., Dong, N., 2019. How contemporary bioclimatic and human controls change global fire regimes. Nature Climate Change 9 (9), 690–696. https://doi.org/10.1038/s41558-019-0540-7.
Lee, L., Zhang, P., Qi, C., Hu, X., Gu, M., 2019. HIRAS noise performance improvement based on principal component analysis. Appl. Optics 58 (20), 5506. https://doi.org/10.1364/AO.58.005506.
Liu, X., Smith, W.L., Zhou, D.K., Larar, A., 2006. Principal component-based radiative transfer model for hyperspectral sensors: theoretical concept. Appl. Optics 45 (1), 201. https://doi.org/10.1364/AO.45.000201.
Morisette, J.T., Giglio, L., Csiszar, I., Setzer, A., Schroeder, W., Morton, D., Justice, C.O., 2005. Validation of *MODIS* active fire detection products derived from two algorithms. Earth Interact. 9 (9), 1–25. https://doi.org/10.1175/EI141.1.
Oliva, P., Schroeder, W., 2015. Assessment of *VIIRS* 375m active fire detection product for direct burned area mapping. Remote Sensing Environ. 160, 144–155. https://doi.org/10.1016/j.rse.2015.01.010.
Pan, F., Huang, X., 2018. The spectral dimension of modeled relative humidity feedbacks in the CMIP5 experiments. J. Climate 31 (24), 10021–10038. https://doi.org/10.1175/JCLI-D-17-0491.1.
Parker, R.J., Boesch, H., Wooster, M.J., Moore, D.P., Webb, A.J., Gaveau, D., Murdiyarso, D., 2016. Atmospheric CH_4 and CO_2 enhancements and biomass burning emission ratios derived from satellite observations of the 2015 Indonesian fire plumes. Atmos. Chem. Phys. 16 (15), 10111–10131. https://doi.org/10.5194/acp-16-10111-2016.
Pearson, K., 1901. LIII. On lines and planes of closest fit to systems of points in space. The London, Edinburgh, and Dublin. Philosophical Magazine and Journal of Science 2 (11), 559–572. https://doi.org/10.1080/14786440109462720.
Rutten, R.J., 2003. Radiative Transfer in Stellar Atmospheres, 8th ed. Sterrekundig Instuut Utrecht, The Netherlands. Retrieved from. https://robrutten.nl/rrweb/rjr-pubs/2003rtsa.book.....R.pdf.
Schroeder, W., Giglio, L., 2017. Visible Infrared Imaging Radiometer Suite (*VIIRS*) 750 M Active Fire Detection and Characterization Algorithm Theoretical Basis Document 1.0. NASA. Retrieved from. https://VIIRSland.gsfc.nasa.gov/PDF/VIIRS_activefire_750m_ATBD.pdf.
Schroeder, W., Giglio, L., 2018. NASA *VIIRS* Land Science Investigator Processing System (SIPS) Visible Infrared Imaging Radiometer Suite (*VIIRS*) 375 M & 750 M Active Fire Products—Product User's Guide Version 1.4. NASA. Retrieved from. https://VIIRSland.gsfc.nasa.gov/PDF/VIIRS_activefire_User_Guide.pdf.
Schroeder, W., Prins, E., Giglio, L., Csiszar, I., Schmidt, C., Morisette, J., Morton, D., 2008. Validation of GOES and *MODIS* active fire detection products using ASTER and ETM+ data. Remote Sensing Environ. 112 (5), 2711–2726. https://doi.org/10.1016/j.rse.2008.01.005.
Serio, C., Masiello, G., Mastro, P., Tobin, D.C., 2020. Characterization of the observational covariance matrix of hyper-spectral infrared satellite sensors directly from measured earth views. Sensors 20 (5), 1492. https://doi.org/10.3390/s20051492.
Simmons, A., et al., 2020. Global stratospheric temperature bias and other stratospheric aspects of ERA5 and ERA5.1. In: ECMWF Technical Memoranda #859. https://doi.org/10.21957/rcxqfmg0.
Smith, N., Barnet, C.D., 2020. CLIMCAPS observing capability for temperature, moisture, and trace gases from AIRS/AMSU and CrIS/ATMS. Atmos. Meas. Tech. 13, 4437–4459. https://doi.org/10.5194/amt-13-4437-2020.
Susskind, J., Barnet, C.D., Blaisdell, J.M., 2003. Retrieval of atmospheric and surface parameters from *AIRS*/AMSU/HSB data in the presence of clouds. IEEE Trans. Geosci. Remote Sens. 41, 390–409.
Tobin, D.C., Antonelli, P.B., Revercomb, H.E., Dutcher, S.T., Turner, D.D., Taylor, J.K., Knuteson, R.O., Vinson, K.H., 2007. Hyperspectral data noise characterization using principle component analysis: application to the atmospheric infrared sounder. J. Appl. Remote Sensing 1 (1), 013515. https://doi.org/10.1117/1.2757707.
Tobin, D., et al., 2013. Suomi-NPP *CrIS* radiometric calibration uncertainty. J. Geophys. Res. Atmos. 118, 10,589–10,600. https://doi.org/10.1002/jgrd.50809.
Touma, D., Stevenson, S., Lehner, F., Coats, S., 2021. Human-driven greenhouse gas and aerosol emissions cause distinct regional impacts on extreme fire weather. Nat. Commun. 12 (1), 212. https://doi.org/10.1038/s41467-020-20570-w.
Tremblay, D.A., Iturbide-Sanchez, F., Chen, Y., Borg, L., Predina, J., Jin, X., Tobin, D.C., Strow, L., Mooney, D.L., Johnson, D., Suwinski, L., Revercomb, H.E., 2022. Radiometric noise assessment of the cross-track infrared sounder on the NOAA-20 satellite. IEEE Trans. Geosci. Remote Sensing 60, 1–15. https://doi.org/10.1109/TGRS.2021.3083137.
Turner, D.D., Knuteson, R.O., Revercomb, H.E., Lo, C., Dedecker, R.G., 2006. Noise reduction of atmospheric emitted radiance interferometer (AERI) observations using

principal component analysis. J. Atmos. Oceanic Tech. 23 (9), 1223–1238. https://doi.org/10.1175/JTECH1906.1.

UW-Madison Space Science and Engineering Center: Hank Revercomb; UMBC Atmospheric Spectroscopy Laboratory: Larrabee Strow, 2020. Suomi NPP *CrIS* Level 1B Full Spectral Resolution V3, Greenbelt, MD, Goddard Earth Sciences Data and Information Services Center (GES DISC). Accessed: July 2023. https://doi.org/10.5067/ZCRSHBM5HB23.

Vitolo, C., Di Giuseppe, F., Barnard, C., Coughlan, R., San-Miguel-Ayanz, J., Libertá, G., Krzeminski, B., 2020. ERA5-based global meteorological wildfire danger maps. Scientific Data 7 (1), 216. https://doi.org/10.1038/s41597-020-0554-z.

Vu Van, A., Boynard, A., Prunet, P., Jolivet, D., Lezeaux, O., Henry, P., Camy-Peyret, C., Clarisse, L., Franco, B., Coheur, P.-F., Clerbaux, C., 2023. Near-real-time detection of unexpected atmospheric events using principal component analysis on the infrared atmospheric sounding interferometer (IASI) radiances. Atmos. Meas. Tech. 16 (8), 2107–2127. https://doi.org/10.5194/amt-16-2107-2023.

Wang, L., Tremblay, D., Zhang, B., Han, Y., 2016. Fast and accurate collocation of the visible infrared imaging radiometer suite measurements with cross-track infrared sounder. Remote Sens. (Basel) 8 (1), 76. https://doi.org/10.3390/rs8010076.

Wang, X., Parisien, M.-A., Taylor, S.W., Candau, J.-N., Stralberg, D., Marshall, G.A., Little, J.M., Flannigan, M.D., 2017. Projected changes in daily fire spread across Canada over the next century. Environ. Res. Lett. 12 (2), 025005 https://doi.org/10.1088/1748-9326/aa5835.

Watson, R.T., Noble, I.R., Bolin, B., Ravindranath, N.H., Verardo, D.J., Dokken, D.J., 2000. Land Use, Land-Use Change, and Forestry: A Special Report of the Intergovernmental Panel on Climate Change. Cambridge University Press, Cambridge, UK.

Wooster, M., Zhukov, B., Oertel, D., 2003. Fire radiative energy for quantitative study of biomass burning: derivation from the BIRD experimental satellite and comparison to *MODIS* fire products. Remote Sensing Environ. 86 (1), 83–107. https://doi.org/10.1016/S0034-4257(03)00070-1.

Wooster, M.J., Xu, W., Nightingale, T., 2012. Sentinel-3 SLSTR active fire detection and FRP product: pre-launch algorithm development and performance evaluation using *MODIS* and ASTER datasets. Remote Sens. Environ. 120, 236–254. https://doi.org/10.1016/j.rse.2011.09.033.

Worden, H.M., Francis, G.L., Kulawik, S.S., Bowman, K.W., Cady-Pereira, K., Fu, D., Hegarty, J.D., Kantchev, V., Luo, M., Payne, V.H., Worden, J.R., Commane, R., McKain, K., 2022. TROPESS/*CrIS* carbon monoxide profile validation with NOAA GML and ATom in situ aircraft observations. Atmos. Meas. Tech. 15 (18), 5383–5398. https://doi.org/10.5194/amt-15-5383-2022.

Xiong, X., Liu, X., Wu, W., Knowland, K.E., Yang, Q., Welsh, J., Zhou, D.K., 2022. Satellite observation of stratospheric intrusions and ozone transport using *CrIS* on SNPP. Atmos. Environ. 273, 118956 https://doi.org/10.1016/j.atmosenv.2022.118956.

Yu, J., Jiang, X., Zeng, Z.-C., Yung, Y.L., 2024. Fire monitoring and detection using brightness-temperature difference and water vapor emission from the atmospheric infrared sounder. J. Quant. Spectrosc. Radiat. Transf. 317, 108930 https://doi.org/10.1016/j.jqsrt.2024.108930.

Yue, Q., Lambrigtsen, B., 2019. AIRS V7 L2 Performance Test and Validation Report. available at: https://docserver.gesdisc.eosdis.nasa.gov/public/project/*AIRS*/V7_L2_Performance_Test_and_Validation_report.pdf.

Yue, Q., Kahn, B.H., Fetzer, E.J., Teixeira, J., 2011. Relationship between marine boundary layer clouds and lower tropospheric stability observed by *AIRS*, CloudSat, and CALIOP. J. Geophys. Res. 116 (D18), D18212. https://doi.org/10.1029/2011JD016136.

Yue, Q., Fetzer, E.J., Kahn, B.H., Wong, S., Manipon, G., Guillaume, A., Wilson, B., 2013. Cloud-state-dependent sampling in *AIRS* observations based on CloudSat cloud classification. J. Climate 26 (21), 8357–8377. https://doi.org/10.1175/JCLI-D-13-00065.1.

Yue, Q., Fetzer, E.J., Wang, L., Kahn, B.H., Smith, N., Blaisdell, J.M., Meyer, K.G., Schreier, M., Lambrigtsen, B., Tkatcheva, I., 2022. Evaluating the consistency and continuity of pixel-scale cloud property data records from Aqua and SNPP (Suomi National Polar-orbiting Partnership). Atmos. Meas. Tech. 15 (7), 2099–2123. https://doi.org/10.5194/amt-15-2099-2022.

Zavyalov, V., et al., 2013. Noise performance of the *CrIS* instrument. J. Geophys. Res. Atmos. 118, 13,108–13,120. https://doi.org/10.1002/2013JD020457.